Nano Research

ISSN 1998-0124 CN 11-5974/O4
https://doi.org/10.26599/NR.2026.94909269

Research Article

Raman spectra of van der Waals layered $MoSi_2N_4$ and WSi_2N_4

Chen Chen[1,2], Dayong Yang[1,2], Xiaoqiao Hu[1,2], Yan Liang[1], Chuan Xu[1,2](✉), Wencai Ren[1,2](✉)

[1] Shenyang National Laboratory for Materials Science, Institute of Metal Research, Chinese Academy of Sciences, Shenyang 110016, China

[2] School of Materials Science and Engineering, University of Science and Technology of China, Shenyang 110016, China

Nano Res., **Just Accepted Manuscript** • https://doi.org/10.26599/NR.2026.94909269

https://www.sciopen.com/journal/1998-0124 on Oct. 19, 2026

© The Authors(s)

Just Accepted

This is a "Just Accepted" manuscript, which has been examined by the peer-review process and has been accepted for publication. A "Just Accepted" manuscript is published online shortly after its acceptance,which is prior to technical editing and formatting and author proofing. Tsinghua University Press (TUP) provides "Just Accepted" as an optional and free service which allows authors to make their results available to the research community as soon as possible after acceptance. After a manuscript has been technically edited and formatted, and the page proofs have been corrected, it will be removed from the "Just Accepted" web site and published officially with volume and article number (e.g., *Nano Research*, **2025**, *18*, 94906990). Please note that technical editing may introduce minor changes to the manuscript text and/or graphics which may affect the content, and all legal disclaimers that apply to the journal pertain. In no event shall TUP be held responsible for errors or consequences arising from the use of any information contained in these "Just Accepted" manuscripts. To cite this anuscript please use its Digital Object Identifier (DOI®),which is identical for all formats of publication.

Just Accepted

Research Article

Raman spectra of van der Waals layered $MoSi_2N_4$ and WSi_2N_4

Chen Chen[1,2], Dayong Yang[1,2], Xiaoqiao Hu[1,2], Yan Liang [1], Chuan Xu[1,2], Wencai Ren[1,2]**

[1]Shenyang National Laboratory for Materials Science, Institute of Metal Research, Chinese Academy of Sciences, Shenyang 110016, China

[2]School of Materials Science and Engineering, University of Science and Technology of China, Shenyang 110016, China

Received: 11 July 2026; **Revised:** 12 September 2026; **Accepted:** 19 October 2026

✉Address correspondence to Wencai Ren, wcren@imr.ac.cn; Chuan Xu, xuc@imr.ac.cn

Cite this article: *Nano Research*, 2026, 19, 94909269 https://doi.org/10.26599/NR.2026.94909269

Just Accepted

ABSTRACT

Raman spectroscopy, as a rapid, nondestructive and powerful technique, has been widely used to study two-dimensional (2D) materials. The emerging 2D van der Waals layered MSi_2N_4 (M = Mo or W) semiconductors show remarkable electrical, optical, thermal, and mechanical properties. However, their Raman signatures and defect-related features remain poorly understood. Here, we use first-principles calculations and Raman spectroscopy to investigate the Raman spectra of MSi_2N_4. The first-order phonon modes are unambiguously assigned, while most of the second- order Raman peaks are preliminarily identified. Furthermore, we observe an anomalous Davydov splitting in multilayer samples, suggesting a distinctive interlayer vibrational coupling. By controllably introducing defects into MSi_2N_4, defect-activated Raman features are identified, providing a practical nondestructive approach for crystal quality assessment. This work offers foundational insights into the Raman spectra of $MoSi_2N_4$ and WSi_2N_4, enabling rapid and nondestructive structural characterization and facilitating their controlled synthesis.

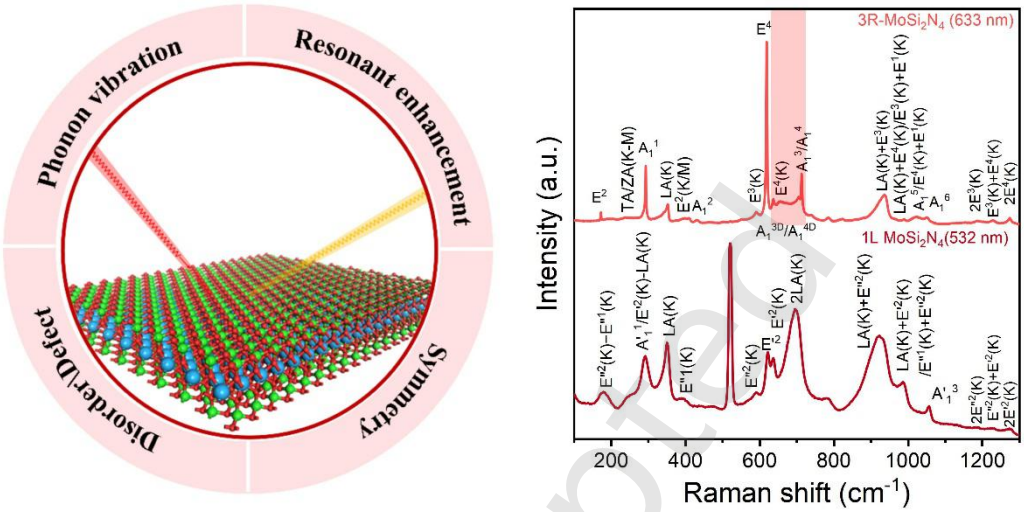
KEYWORDS

$MoSi_2N_4$, WSi_2N_4, Raman spectroscopy, phonon vibration, defect

Just Accepted

Table of Contents

Raman Spectra of MSi_2N_4



First-principles calculations and Raman spectroscopy preliminarily reveal the intrinsic vibrational and defect-activated Raman features of two-dimensional van der Waals layered $MoSi_2N_4$ and WSi_2N_4, and uncover a potential anomalous Davydov splitting. This work provides a foundation for fast structural identification and material quality assessment.

Just Accepted

1 Introduction

In the past two decades, two-dimensional (2D) materials have attracted tremendous interest due to their remarkable quantum confinement effect and huge specific surface area, and hold promise for intriguing applications, including electronics, optoelectronics and energy technology [1, 2]. Raman spectroscopy, as a rapid and nondestructive characterization method, plays an essential role in the structure analysis of 2D materials by correlating phonon vibration with the structural characteristics [3]. For example, the intrinsic G band in graphene corresponds to the in-plane vibration of carbon with sp^2 hybridization, while the D band stems from the disorders in the lattice [4]. The intensity ratio of D and G, I_D/I_G, has been widely used to estimate the crystalline quality qualitatively [4]. Moreover, the layer number and stacking of 2D materials can be identified through analyzing the shift and profile of the feature peak or the intensity ratio of two specific peaks [5, 6]. With the rapid development of 2D materials, Raman spectroscopy has enabled detailed structural characterization (e.g., layer number [5,6], defect identification [5,7], polytypism [8], and heterostructure [9]), and provided insights into physical properties such as doping type [10,11], interlayer coupling [12, 13], magnetism [14] and thermal properties [15].

The $MoSi_2N_4$ materials family is a recently emerging class of van der Waals (vdW) layered materials with a general formula MA_2Z_4, encompassing metals, semiconductors, superconductors, topological insulators, ferroelectrics and ferromagnets, owing to the diversity of elements and structures in MA_2Z_4 [16, 17]. Among this family, $MoSi_2N_4$ and WSi_2N_4 have been synthesized by chemical vapor deposition (CVD) and they both are high-performance p-type semiconductors with high intrinsic carrier mobility, excellent thermal conductivity, remarkable mechanical strength, and outstanding environmental stability [16, 18]. To date, the structural characterization of MSi_2N_4 has relied primarily on transmission electron microscopy, which provides distinct atomic-scale structural information but is time-consuming and

Just Accepted

typically limited to nanometer-level regions. Although Raman spectra of monolayer (1L) $MoSi_2N_4$ have been reported in both theory and experiments [16, 19, 20], discrepancies between experimental data and theoretical predictions persist. For example, the observed prominent peaks at 350 and 926 cm^{-1} in the experiment have not yet been explained by the theoretical calculation. Moreover, defect-related Raman studies for $MoSi_2N_4$ are absent, leaving a gap in the nondestructive assessment of crystal quality. Moreover, though the Raman spectrum of 1L WSi_2N_4 has been obtained under a 325 nm laser, the theoretical analysis and assignment of Raman peaks for WSi_2N_4 are still blank.

Here, we conducted a systematic study of Raman spectra of MSi_2N_4, combining first-principles calculations and Raman spectroscopy. We first clarified the Raman scattering behavior of 1L and multilayer (ML) MSi_2N_4 via symmetry analysis and first-principles calculations. Using CVD-grown 1L and ML MSi_2N_4 crystals as the sample platform, we then measured Raman spectra under multiple excitation wavelengths and polarization configurations to unambiguously assign their first-order phonon modes and elucidate the evolution of symmetry from monolayer to multilayer. Notably, a special Davydov splitting behavior was observed in both ML samples. Furthermore, we identified the defect-activated Raman peaks through defect engineering. Finally, by integrating calculated phonon spectra with experimental results, we provided a preliminary assignment of the second‑order Raman peaks.

2 Results and discussion

2.1 Raman Spectral Assignment of Monolayer $MoSi_2N_4$

Monolayer MSi_2N_4 shows a hexagonal structure with *P-6m2* space group (No. 187) and D_{3h} point group symmetry. It consists of septuple atomic layers, N-Si-N-M-N-Si-N, occupying four inequivalent Wyckoff positions, which are labeled N_{top}, Si, N_{mid}, and Mo in sequence, as shown in Fig. 1(a). N_{top} and N_{mid} denote the

Just Accepted

outer and inner N atoms, respectively. There are seven atoms in the unit cell of 1L MSi_2N_4, resulting in twenty-one phonon vibration modes: three acoustic branches and eighteen optical branches. The phonon dispersion curves of 1L $MoSi_2N_4$ and WSi_2N_4 are shown in Fig. 1(b, c), respectively. At the Γ point of the Brillouin zone, the eighteen optical normal vibrational modes (first-order phonon scattering) can be denoted by the following irreducible representations:

$$\Gamma_{optic} = 3A'_1 + 3A''_2 + 3E' + 3E''$$

where E (E' and E") and A (A'_1 and A''_2) modes correspond to in-plane and out-of-plane vibrations, respectively. Based on their symmetry, the A'_1 ($A'_1{}^1$, $A'_1{}^2$ and $A'_1{}^3$) and E" (E''^1, E''^2 and E''^3) modes are Raman-active, the A''_2 ($A''_2{}^1$, $A''_2{}^2$ and $A''_2{}^3$) modes are infrared-active, and the E' (E'^1, E'^2 and E'^3) modes exhibit both Raman and Infrared activity (Table S1), supported by Bilbao Crystallographic Server [21, 22]. From all eighteen visualized vibration patterns shown in Fig. 1(d), it can be found that each E' mode and E" mode has two degenerate vibration modes, corresponding to vibrations along the zigzag and armchair directions, respectively. Within a backscattering geometry, the intensity of the E" modes is strictly forbidden (Supplementary Note 1). Therefore, it is predicted that six first-order phonon scattering peaks will be detected, including $A'_1{}^1$, $A'_1{}^2$, $A'_1{}^3$, E'^1, E'^2 and E'^3. Their Raman scattering process is shown in Fig. 1(e) (i). Additionally, second-order phonon processes may also occur, including overtone modes (2X), defect-induced modes (D), and combination modes (X_1+X_2), and their Raman scattering processes are shown in Fig. 1(e) ii-iv.

Just Accepted

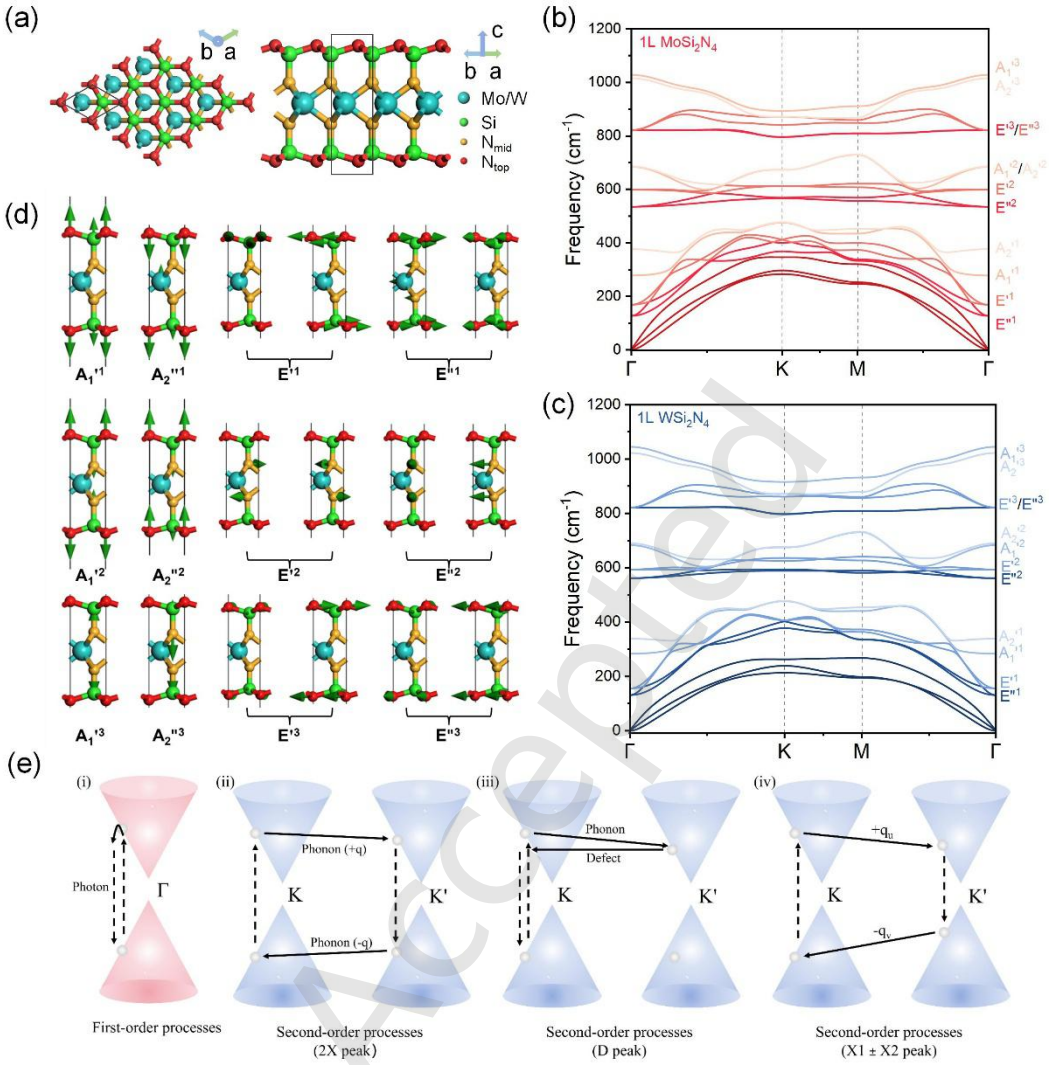
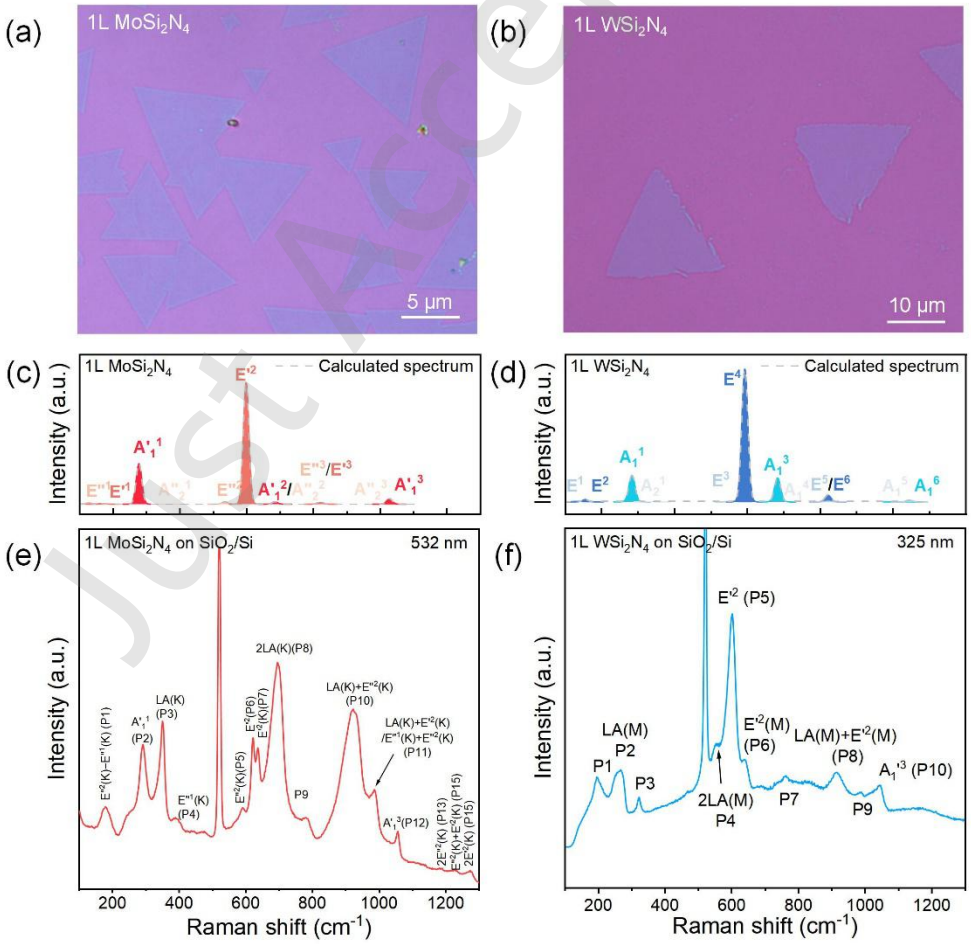


Fig. 1 Crystal structure and phonon analysis of 1L MSi_2N_4. (a) Schematic crystal structure of 1L MSi_2N_4. (b, c) Phonon dispersion relations of 1L $MoSi_2N_4$ (b) and 1L WSi_2N_4 (c). (d) Schematic illustrations of the atomic displacement patterns in 1L MSi_2N_4. (e) Raman scattering processes: (i) First-order phonon scattering process, (ii~iv) second-order phonon processes: (ii) 2X peak, (iii) D peak, (iv) $X_1 \pm X_2$ peak.

The photon energy of the incident laser has a significant impact on the Raman signals of the MSi_2N_4 material. When the photon energy of the incident laser matches the electronic transition energy levels of the material, a resonance-enhanced Raman effect occurs, thereby significantly increasing the intensity of characteristic peaks [23]. Monolayer $MoSi_2N_4$ and WSi_2N_4 are indirect semiconductors, featuring direct transitions at the K point (Fig. S1(a, c)), yielding two pronounced excitonic

Just Accepted

resonances labeled A and B due to the spin-orbit coupling effect [16]. For $MoSi_2N_4$, the UV-vis absorption spectrum showed six absorption peaks (A-H) (Fig. S2a, b) (See Supplementary Note 2 for more details). Notably, the B (521 nm, 2.38 eV) and E (310 nm, 4.0 eV) absorption peaks nearly match the 532 nm and 325 nm lasers used in this study, and possibly match the transition energies at points K and M (Fig. S1b, d), respectively, implying the occurrence of exciton-resonance-enhanced Raman scattering. These resonances will selectively enhance Raman scattering intensity via electron-phonon coupling and modify their polarization selectivity, similar to MoS_2 [24, 25]. For WSi_2N_4, the UV-vis absorption spectrum of 1L WSi_2N_4 shows five absorption peaks (A-E) (Fig. S2c, d), among which the C absorption peak (318 nm) is close to the 325 nm laser, possibly matching the transition energy at the Γ point (Fig. S1c, d). Consequently, a significant Raman resonance enhancement will occur only under 325 nm excitation.



Just Accepted

Fig. 2 Raman spectra of 1L MSi_2N_4. (a, b) Optical images of CVD-grown 1L $MoSi_2N_4$ (a) and WSi_2N_4 (b) domains transferred on SiO_2/Si substrate. (c, d) Calculated Raman spectra of 1L $MoSi_2N_4$ (c) and WSi_2N_4 (d). (e, f) The detected Raman spectra of 1L $MoSi_2N_4$ on SiO_2/Si under 532 nm excitation (e) and WSi_2N_4 on SiO_2/Si under 325 nm excitation (f).

To validate the theoretical predictions, we measured the Raman spectra of CVD-grown 1L $MoSi_2N_4$ and WSi_2N_4 (see Methods for more details). Fig. 2(a) and (b) show 1L $MoSi_2N_4$ and WSi_2N_4 transferred onto SiO_2/Si substrate. Their thicknesses, measured by atomic force microscopy (AFM), were 1.13 nm and 1.16 nm (Fig. S3), respectively, consistent with the reported monolayers [15, 16, 26]. Raman spectra of 1L $MoSi_2N_4$ and WSi_2N_4 were measured under multiple excitation wavelengths (325 nm, 532 nm, 633 nm, and 785 nm), as shown in Fig. S4. For 1L $MoSi_2N_4$, Raman signals can be acquired using 532 nm and 325 nm lasers, whereas for 1L WSi_2N_4, detectable Raman signals are only observed under 325 nm excitation.

Fig. 2(c) shows the Raman spectrum of 1L $MoSi_2N_4$ based on first-principles calculations. It can be observed that three prominent peaks are located at 277.7, 598.6, and 1027.9 cm^{-1}, corresponding to the $A'_1{}^1$, E'^2, and $A'_1{}^3$ modes, respectively (Table S2), consistent with the reported results [19, 20]. However, the intensities of the other three Raman-active modes, $A'_1{}^2$, E'^1 and E'^3, are very weak, potentially precluding their clear observation. Fig. 2(e) shows the Raman spectrum of 1L $MoSi_2N_4$ under 532 nm laser excitation, where 12 significant Raman peaks are displayed. (see Table S2 for more details). For clarity, all detected peaks were labelled by PX in ascending order of frequency. In Fig. 2(e), P2 (290.3 cm^{-1}), P6 (620.9 cm^{-1}), and P12 (1053.3 cm^{-1}) aligned closely with the calculated positions of the $A'_1{}^1$, E'^2, and $A'_1{}^3$ modes, respectively, assigned to these intrinsic zone-center phonons. The other nine peaks (P1, P3, P4, P5, P7-P11 and P13-15) stem from second-order phonon scattering processes (Table S2). Unfortunately, due to the Fröhlich interaction [25], polarized Raman spectroscopy cannot provide further evidence (Fig. S5). Under 325 nm excitation laser, only P3, P6 (E'^2), and P10 were detected (Fig. S4(a)).

Like $MoSi_2N_4$, 1L WSi_2N_4 is theoretically expected to have six identifiable Raman

Just Accepted

characteristic peaks. They are located at 155.4, 283.2, 593.0, 689.7, 821.2, and 1044.6 cm^{-1} in the calculated spectrum, as shown in Fig. 2(d) and Table S3. There are ten peaks in the Raman spectrum of 1L WSi_2N_4 under a 325 nm laser (Fig. 2(f)). P5 and P10 are located at 601.5 and 1043.8 cm^{-1}, respectively, and are in close agreement with the calculated positions of E'^2 and $A'_1{}^3$. The other peaks arise from second-order phonon scattering. The following Raman peak assignments for multilayer MSi_2N_4 provide additional support for those of the monolayer.

2.2 Raman Spectral Assignment of 3R-phase $MoSi_2N_4$ and WSi_2N_4

Raman spectra of multilayer materials usually show layer-number dependence and can reveal the interlayer interaction [5, 12, 27, 28]. The MSi_2N_4 flakes with a lateral size of about ten micrometers, which were synthesized by CVD (Fig. S6(a) and 7(a)) [29]. The stacking configurations of ML $MoSi_2N_4$ and WSi_2N_4 were investigated by atomic- resolution atomic-resolution integrated differential phase contrast scanning transmission electron microscopy (iDPC-STEM) along the ⟨10 10⟩ direction. A periodic shift of $\frac{a}{\sqrt{3}}$ between adjacent layers was observed in Fig. 3(a, b), indicating the ABC stacking order of 3R phase.

Just Accepted

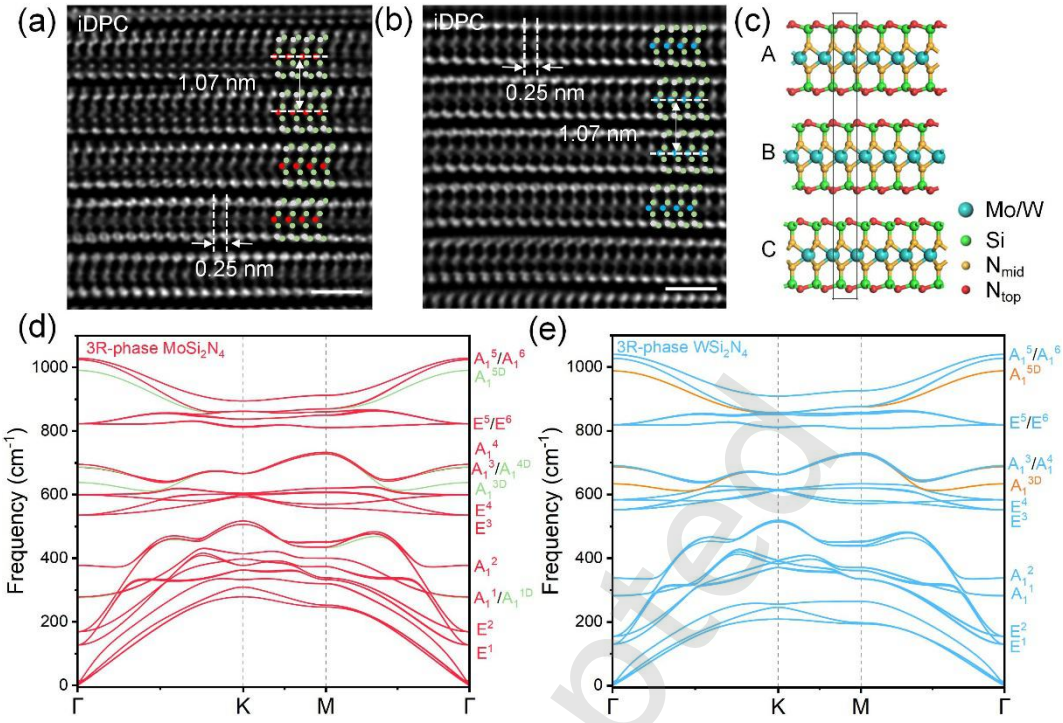


Fig. 3 Crystal structure and phonon analysis of ML MSi_2N_4. (a, b) Cross-sectional iDPC-STEM images of 3R-phase $MoSi_2N_4$ (a) and WSi_2N_4 (b). (c) Schematic crystal structure of 3R-phase MSi_2N_4 with ABC stacking. (d, e) Phonon dispersion relations of 3R-phase $MoSi_2N_4$ (d) and 3R-phase WSi_2N_4 (e), showing Davydov splitting of several A_1 modes (highlighted in green or orange). Scale bars: 1 nm in a and b.

3R-phase MSi_2N_4 belongs to the space group *R3m* (No. 160) with C_{3v} point group symmetry, as schematically shown in Fig. 3(c). The phonon dispersion relations of 3R-phase $MoSi_2N_4$ and WSi_2N_4 are presented in Fig. 3(d, e). Under this C_{3v} symmetry, the irreducible representation for the optical normal modes at the Γ point can be represented as:

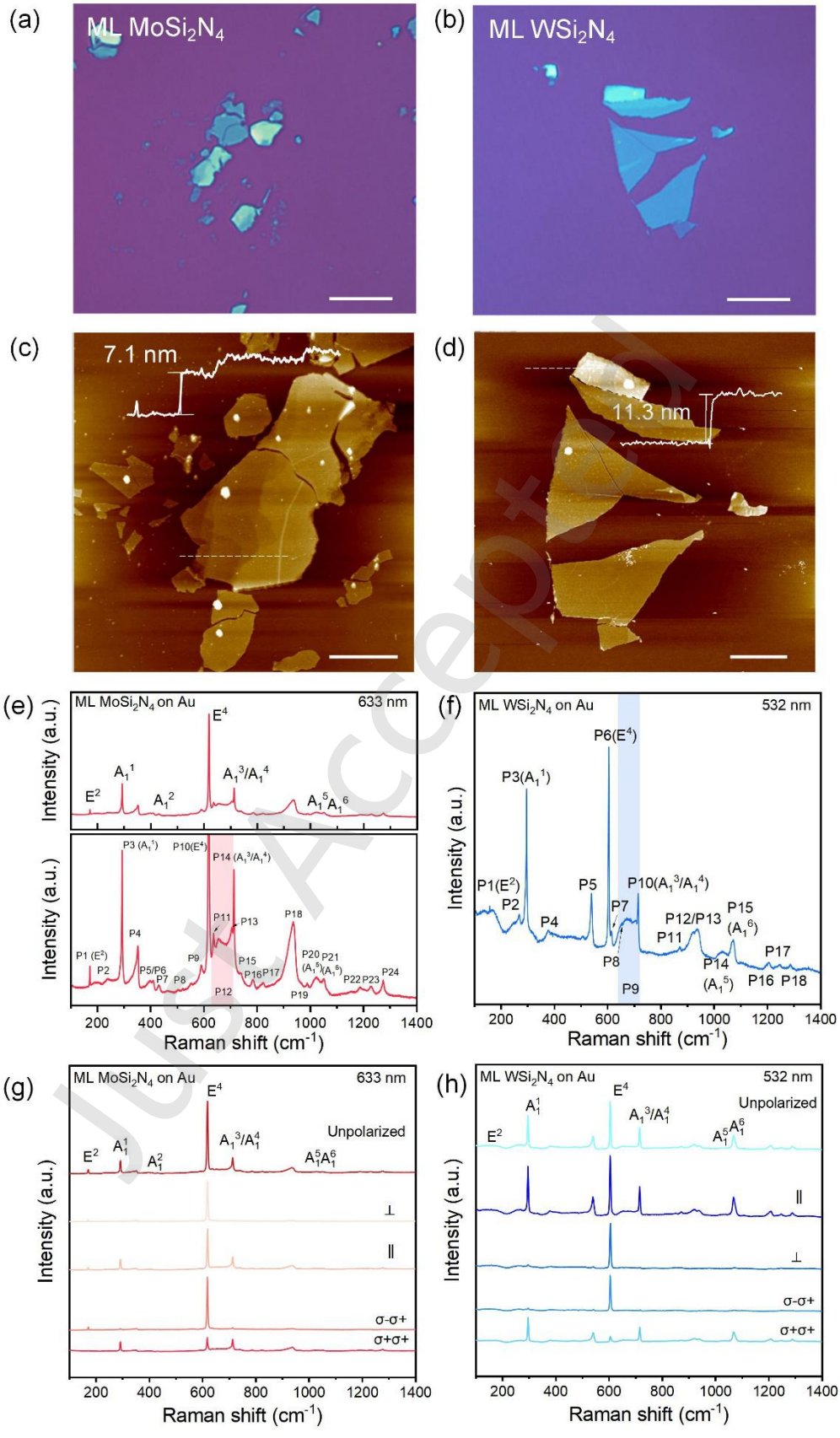
$$\Gamma_{optic}=6A_1+6E$$

All twelve optical modes are both Raman- and infrared-active (Supplementary Note 1 and Table S1) for the 3R-phase MSi_2N_4 unit cell with a periodic three-layer structure, supported by Bilbao Crystallographic Server [21, 22]. The symmetry reduction from

Just Accepted

D_{3h} (1L) to C_{3v} (3R phase) activates specific vibrational modes, similar to 3R-phase NbS_2 [30]. Notably, the three Raman-inactive A''_2 modes in the monolayer become Raman-active in the 3R phase. Although the total phonon branches increase to 63, most peak positions in 3R- phase MSi_2N_4 remain close to those of the monolayer (Tables S2 and S3). However, several distinct branches, highlighted in orange or green and labeled A_1^D, are clearly resolved. These may arise from Davydov splitting of A_1 modes due to interlayer interaction [28]. In addition, E^3 and E^4 are degenerate at the K point.

Just Accepted



Just Accepted

Fig. 4 Morphology characterization and Raman spectra of ML $MoSi_2N_4$ and WSi_2N_4. (a, b) Optical images of ML $MoSi_2N_4$ (a) and WSi_2N_4 (b). (c, d) Atomic force microscope (AFM) images corresponding to ML $MoSi_2N_4$ (c) and WSi_2N_4 (d) flakes shown in (a) and (b), respectively. (e, f) Raman spectra of ML $MoSi_2N_4$ under 633 nm excitation (e) and ML WSi_2N_4 under 532 nm excitation (f). (g, h) Linearly and circularly polarized Raman spectra of ML $MoSi_2N_4$ under 633 nm excitation (g) and ML WSi_2N_4 under 532 nm excitation (h). Scale bars: 10 μm in (a, b), 2 μm in (c) and 5 μm in (d).

Multilayer flakes of ML MSi_2N_4, with thicknesses ranging from a few nanometers to tens of nanometers, were obtained via mechanical exfoliation (Fig. 4(a~d) and S8). Under multiple excitation wavelengths (325, 532, 633, and 785 nm), the multilayer structures exhibit distinct Raman signals (Fig. S9(a, b)). Here, the Au substrate was employed because it provides a flat background without any interfering peaks (Fig. S10). Specifically, the Raman spectrum of ML $MoSi_2N_4$ acquired with a 532 nm laser is similar to that of the monolayer and also undergoes resonance enhancement. In contrast, 1L $MoSi_2N_4$ and WSi_2N_4 almost show no Raman response under non-resonant excitation. This absence may be attributed to its low Raman intensity and scattering efficiency, which may arise from its strong ionic bond characteristics, similar to the case of *h*-BN [31].

The Raman spectra of ML $MoSi_2N_4$ are more complex than those of the monolayer. Under 633 nm excitation, seven first-order peaks were detected for ML $MoSi_2N_4$ (Fig. 4(e)). The peaks P1, P3, P10, P14, P20 and P21 are assigned to E^2, A_1^1, E^4, A_1^3/A_1^4, A_1^5 and A_1^6 modes (see Table S2), with reference to the theoretically calculated peak positions of first-order Raman scattering, corresponding to the E'^1, $A'_1{}^1$, E'^2, $A''_2{}^2/A'_1{}^2$, and $A''_2{}^3$ and $A'_1{}^3$ modes in 1L $MoSi_2N_4$. Among them, $A''_2{}^2$ and $A''_2{}^3$ modes were suppressed in the monolayers. In addition to these first-order peaks, seventeen peaks are observed, which likely originate from second‑ order phonon scattering processes. For example, P24 (1274.1 cm^{-1}) corresponds to the overtone of P11 located at 637.2 cm^{-1}, similar to the D and 2D peak of graphene [5]. As shown in Fig. S11, several

Just Accepted

peaks (notably P4, P9, P11, P12, P13, P18-20, P22-24) exhibit a pronounced enhancement of intensity under 532 nm excitation, due to the exciton resonance enhancement effect (Table S2). Since the laser energy matches the exciton transition energy near K point, these peaks may be related to the scattering process at the K point [32]. Additionally, a broad spectral feature appears in the 630-710 cm^{-1} region, which will be discussed in detail later.

To unambiguously assign the Raman characteristic peaks of 3R-phase MSi_2N_4, we performed polarized Raman spectroscopy using both linear and circular polarization configurations. The schematic of the experimental setup is shown in Fig. S12. The polarization selection rules are summarized in Supplementary Note 1 and the polarization activity of the first-order Raman vibration is shown in Table 1. To avoid the misleading effects of exciton resonance, we collected polarized Raman spectra of ML $MoSi_2N_4$ under non- resonant 633 nm excitation (Fig. 4(g), S13 and S14). The results aligned closely with the theoretical analysis. Specifically, in the cross-linear configuration (⊥), all as-identified first-order A_1 peaks (P3, P13, P14, P20, P21) are suppressed. In addition, P2, P5-8, P12, P13, P15-19, P22-24, and the 630-710 cm^{-1} band-like peak were also suppressed, suggesting their A_1 mode character. In the circular configurations, P1 and P10 show strong suppression under co-circular polarization (σ+σ+), further confirming the identification of E^2 and E^4 modes. Meanwhile, the cross-circular spectra (σ-σ+) exhibit a mode activity pattern similar to that observed under cross-linear polarization (∥). The three peaks P4, P9, and P11 exhibit no polarization selectivity under either linear or circular polarization. Based on subsequent characterization and theoretical calculations, most of the second- order peaks have been preliminarily identified (see Supplementary Note 3 for more details).

Table 1: Polarization activity of the first-order Raman vibration

Raman mode	Linearly polarized		Circularly polarized	
	$I_{\parallel}$	$I_{\perp}$	$I_{\sigma-\sigma+}$	$I_{\sigma+\sigma+}$
A'_1	a^2	0	a^2	0

Just Accepted

E'	a^2	c^2	0	c^2
A_1	e^2	0	e^2	0
E	e^2	g^2	0	g^2

Calculated phonon dispersion curves, combined with polarized Raman spectroscopy measurements, were employed to identify the vibrational modes of ML WSi_2N_4 (Fig. 4(f, h) and S15-17). Six first-order peaks (P1, P3, P6, P11, P15 and P16), located at 158.9, 296.2, 604.5, 714.9, 1031.0, and 1072.6 cm^{-1}, show good agreement with theoretically predicted first-order modes, corresponding to E^2, A_1^1, E^4, A_1^3/A_1^4, A_1^5 and A_1^6 at calculated positions of 155.0, 282.9, 583.6, 687.0/690.5, 1027.2 and 1039.7 cm^{-1}, respectively (Table S3). Many peaks (P5, P9, P12-14, P17-18) and the broad band-like feature centered at 630-720 cm^{-1} exhibit A_1 symmetry. The peaks P2 and P4 exhibit no linear or circular polarization selectivity.

Davydov splitting is commonly observed in multilayer vdW layered materials, arising from interlayer vdW interactions and vibrational coupling, such as in transition metal dichalcogenides [28, 33, 34] and $NiPS_3$ [35]. Here, an anomalously large Davydov splitting is observed in MSi_2N_4, deviating from the conventional expectation that high-frequency modes exhibit smaller Davydov splitting than low-frequency modes [12, 28]. In 3R-phase $MoSi_2N_4$, however, certain high-frequency A_1 modes exhibit exceptionally large splitting. Specifically, the A_1^3 mode reaches 48.0 cm^{-1} (Fig. 3(d)), approximately six times the typical ~7.0 cm^{-1} value for high-frequency modes in MoS_2 [34], while others remain minimal (see Table S3 for detailed values). This anomalous splitting was observed experimentally as a broad band highlighted in Fig. 4(e,f), which matches calculated Davydov components (A_1^{3D}~A_1^4). Low-temperature Raman measurements at 78 K on a 9L flake (Fig. S18b) failed to resolve the Davydov splitting. Under non-resonant conditions, the signal was too weak, whereas under resonant conditions the 2LA(K) mode masked the Davydov splitting component. This broad band also exhibits the polarization selectivity of A_1 mode (Fig. 4(g,h)). The abnormal Davydov splitting is further supported by reported

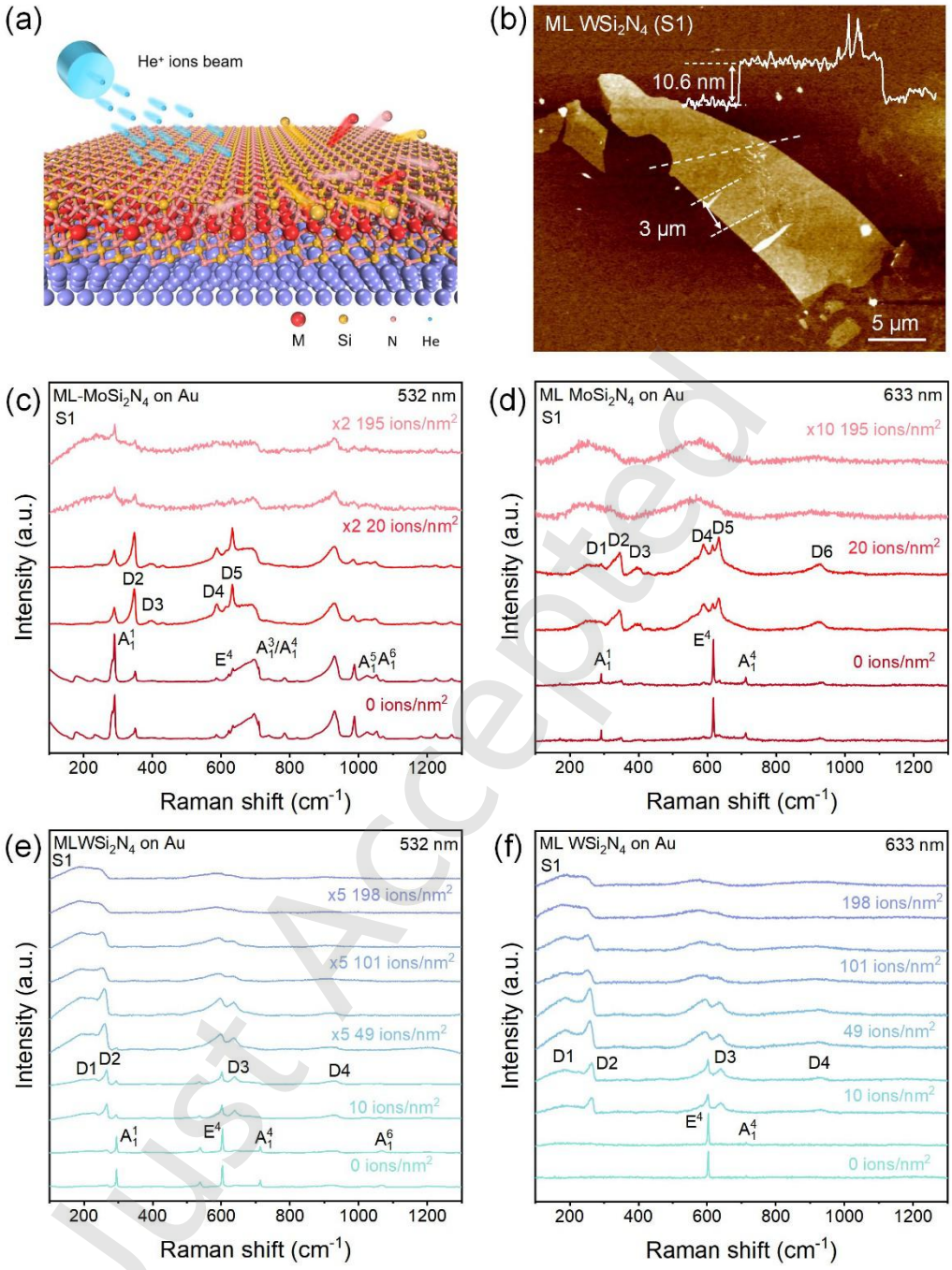
Just Accepted

calculated phonon dispersions [20], ruling out second-order phonon scattering 2LA(K). More details are given in Supplementary Note 4.

2.3 Defect-Activated Raman Modes via Ion Irradiation

Defect-activated Raman peaks in materials play a very important role in rapid quality assessment. To systematically investigate defect-activated Raman peaks in MSi_2N_4, we introduced defects controllably using a focused helium ion beam. This technology has been widely used in other 2D materials, such as graphene [36] and MoS_2 [7]. A helium ion beam would break the lattice of MSi_2N_4 with high energy (Fig. 5(a)), and defect concentration can be controlled by irradiation dose. ML MSi_2N_4 was used for stronger and more uniform Raman signals, and was placed on Au- coated SiO_2/Si substrates to suppress Si background. Considering the laser spot size (~1 μm) and the convenience of measurement, the typical irradiated MSi_2N_4 flake is shown in Fig. 5(b), with an irradiation width of 3 μm. Raman spectra were collected using 532 and 633 nm lasers to track the spectral evolution during the increase of defect density.

Just Accepted



Just Accepted

Fig. 5 Defect-activated Raman spectra of MSi_2N_4. (a) Schematic of He^+ ion beam irradiation on MSi_2N_4. (b) AFM image of a ML WSi_2N_4 flake transferred on an Au-coated SiO_2/Si substrate after irradiation, showing a 3 μm-width irradiated region at a dose of 198 ions/nm^2. (c, d) Evolution of typical Raman spectra of ML $MoSi_2N_4$ with irradiation dose under 532 nm (c) and 633 nm (d) excitation. (e, f) Evolution of

typical Raman spectra of ML WSi_2N_4 with irradiation dose under 532 nm (e) and 633 nm (f) excitation.

Raman spectra for irradiated ML $MoSi_2N_4$ were collected using 633 nm and 532 nm lasers, as shown in Fig. 5(c, d), respectively. With increasing dose, the intensities of the first-order peaks A_1^1, E^4, A_1^3/A_1^4, A_1^5, and A_1^6 diminished gradually and the shape broadened significantly, indicating the degradation of crystal quality [7]. The E^4 peak shows a measurable blue shift under a 633 nm laser, consistent with expectations from the phonon dispersion relation (Fig. 3(d)). The excessive weakening and interference of the other first-order modes prevented reliable analysis of their peak positions. Six defect-activated characteristic peaks were detected at 633 nm (labeled D1-D6), located at 237.8-295.4, 348.1, 392.4-404.7, 591.9, 632.6 and 927.0 cm^{-1}, and four of the peaks (D2-D5) were detected at 532 nm (Table S2). Their intensities first increased and then decreased with increasing dose, similar to the evolution of defect-related peaks in MoS_2 [7]. Among them, D1 and D3 manifest as broad bands. The positions of D2, D3, D5, and D6 peaks show a systematic blue shift with increasing defect concentration, whereas the D4 peak remained stationary (Fig. S20). More samples were measured and showed consistent results (Fig. S21).

The phenomenon of exciton resonance enhancement provides a reference for the scattering centers of defect-phonon scattering and their scattering processes are shown in Fig. 1(e) iii. For ML $MoSi_2N_4$, four defect peaks (D2-D5) are observable under 532 nm excitation (Fig. 5(c)), while two additional peaks (D1 and D6) emerge under 633 nm excitation (Fig. 5(d)). Based on resonance selectivity [37], D2, D3, D4, and D5 are mainly attributed to phonon scattering near the K point coupled with defects, whereas D1 and D6 are more likely associated with scattering at the M point. By referencing the measured peak positions, calculated phonon dispersions, and dose-dependent peak shifts, we tentatively assign D2 (348.1 cm^{-1}), D4 (591.9 cm^{-1}), D5 (632.6 cm^{-1}), and D6 (927.0 cm^{-1}) to the LA(K), E^3(K) mode (568.8 cm^{-1}), E^4(K) mode (604.3 cm^{-1}), and A_1^6(M) mode (910.9 cm^{-1}), respectively. D1 and D3 appear as broad bands, likely involving multiple defect-activated Raman scattering processes,

Just Accepted

and are tentatively assigned to ZA/TA(M–K) and E^1(M–K) (Fig. S22). Through the elemental-projected phonon analysis, the correlation between these peaks and defect sites was tentatively revealed. As shown in Fig. S23, D1 and D2 may originate from Mo-site defects, the D3 band from Si-site defects, and D4, D5, and D6 from N_{mid} site defects. It's worth noting that D2, D4 and D5 can be detected in the unirradiated region of the same flake, suggesting that the defects related to Mo- and N-site form more easily during the CVD growth. This reflects their lower formation energies, consistent with reported literature [38, 39].

The Raman spectral evolution of ML WSi_2N_4 is shown in Fig. 5(e, f) and S24, similar to that of ML $MoSi_2N_4$. Under both 532 nm and 633 nm excitation, four defect-activated features (D1–D4) are detectable in ML WSi_2N_4, with a systematic blueshift (Fig. S25, 26 and Table S3). The D1 band (189.3-242.3 cm^{-1}) is attributed to vibrations along the M–K path involving ZA and TA modes (194-246 cm^{-1}) (Fig. S26). D2 (266.4 cm^{-1}) is assigned to the LA(K) mode near 255.2 cm^{-1}. Both D1 and D2 are tentatively associated with W-site defects (Fig. S27). D3 (640.0 cm^{-1}) and D4 (923.6 cm^{-1}) are tentatively assigned to the E^4(K) mode (~624.5 cm^{-1}) and A_1^6(M) (931.7 cm^{-1}), respectively, tentatively related to N_{mid} site defects. Interestingly, the intensities of the characteristic peaks associated with N_{top} sites and Si sites are relatively low in both $MoSi_2N_4$ and WSi_2N_4, which may be attributed to the strong Si-N bonds. Moreover, it's suggested that the intensity ratio of A_1^1 or E^4 and D ($I_{A_1^1}/I_D$ or I_{E^4}/I_D) in both $MoSi_2N_4$ and WSi_2N_4 can be used to assess the concentration of corresponding defects qualitatively (Fig. S28 and Supplementary Note 5).

The first-order Raman peaks and defect-activated peaks were analyzed and assigned, further combined with calculated phonon dispersions and resonance-enhanced Raman phenomena, providing a reference for identifying overtone modes (2X) and combination modes ($X_1 \pm X_2$) in Fig. 1(e) ii and iv. For example, in the spectra of ML $MoSi_2N_4$, (Fig.S29 (b,c)), the defect-activated peaks D2 (LA(K), P4, 352.1 cm^{-1}), D3 (E^2(K), P5/P6, 398.4/409.2 cm^{-1}), D4 (E^3(K), P9,

Just Accepted

591.2 cm^{-1}), and D5 (E^4(K), P11, 637.2 cm^{-1}) is attributed to phonon–defect scattering. Their corresponding overtone modes, phonon-phonon scattering, are assigned to P9 (705.1 cm^{-1}), P22 (1187.5 cm^{-1}), and P24 (1274.1 cm^{-1}), respectively. Consequently, P9, P22, and P24 are identified as 2LA(K), $2E^3$(K), and $2E^4$(K), respectively. The combination modes are tentatively identified as P18 (930~936 cm^{-1}, LA(K) + E^3(K)), P19 (988.1 cm^{-1}, LA(K) + E^4(K)/E^2(K) + E^3(K)), and P23 (1227.8 cm^{-1}, E^3(K) + E^4(K)). The corresponding difference modes tentatively set as E^4(K) - E^2(K)/E^3(K) - LA(K) (239.1 cm^{-1}), E^3(K) -E^2(K) (178.9 cm^{-1}). The E^4(K) - LA(K) and the E^4(K) + E^2(K) modes overlap with the A_1^1, A_1^5 and A_1^6 modes, while the E^3(K) -E^4(K) mode lies outside the measured spectral range. Furthermore, D6 peak (A_1^6(M) 927.0 cm^{-1}) overlaps P18 (930~936 cm^{-1}, LA(K) + E^3(K)). More detailed assignments of the observed Raman peaks of MSi_2N_4 are provided in Supplementary Note 3, Tables S2–S3 and Fig. S29.

3 Conclusions

In summary, this work presented a systematic Raman spectrum study of 1L and 3R-phase $MoSi_2N_4$ and WSi_2N_4. By integrating theoretical simulations and experimental measurements, we have assigned the primary characteristic Raman peaks for both materials, including first-order phonon scattering peaks (e.g., A_1'/A_1, E'/E for monolayers and multilayers, respectively) and some second-order phonon scattering peaks (e.g., 2LA(K)). An anomalous Davydov splitting behavior is observed and analyzed in the multilayer structures. Furthermore, defect-activated Raman peaks are identified by combining controlled helium-ion irradiation, thereby providing a practical method for non‑ destructive assessment of crystal quality. These findings significantly advance the fundamental understanding of Raman spectra of $MoSi_2N_4$ and WSi_2N_4, and provide a spectroscopic foundation in the synthesis and application in advanced electronic devices.

Just Accepted

4 Methods

4.1 First-Principles Calculations.

The first-principles calculations were carried out using the Vienna Ab initio Simulation Package (VASP) [40, 41] with the projected augmented wave (PAW) method [42] and generalized gradient approximation with the Perdew-Burke-Ernzerhof exchange-correlation functional (GGA-PBE) [43, 44]. The plane-wave cutoff energy of 600 eV was used. A large vacuum space was set to 20 Å. Structures were optimized with a 24 × 24 × 1 k-mesh, convergence criteria of 10^{-8} eV for energy and 10^{-8} eV/Å for forces. Van der Waals corrections were included using Grimme's DFT-D3 [45]. Band structure calculations were performed including spin–orbit coupling. The joint density of states (JDOS) was obtained based on the band structure using VASPKIT package [46]. Phonon dispersions and Raman spectra were calculated using Phonopy [47], Phono3py package, and Phonopy-Spectroscopy package [48] with the finite displacement method (3 × 3 × 1 k-mesh, 10^{-6} eV/Å force convergence). A 4 × 4 × 1 supercell was used for monolayers and a 2 × 2 × 2 supercell for the 3R phase.

4.2 Growth and Transfer of $MoSi_2N_4$ and WSi_2N_4.

1L and ML $MoSi_2N_4$ and WSi_2N_4 crystals were grown using our previously reported CVD methods [16, 26, 29]. In detail, triangular 1L $MoSi_2N_4$ and WSi_2N_4 domains were grown on solid Cu/Mo and liquid Au/W substrates, respectively. Then they were transferred using a PMMA-assisted wet etching method. Multilayer domains were grown by increasing the growth temperature and the supply of nitrogen source. Subsequently, multilayer nanosheets were mechanically exfoliated using silicone-free adhesive plastic films (ULTRON SYSTEMS, INC.) onto target substrates.

4.3 Structural Characterization.

Just Accepted

The morphology and thickness of MSi_2N_4 were characterized using an optical microscope (Nikon LV100D) and atomic force microscopy (AFM, MultiMode VIII, Bruker, Inc.). UV-vis absorption spectra were measured using a Varian Cary 5000 spectrometer. The high-angle annular dark field (HAADF), iDPC, differential phase contrast (dDPC) scanning transmission electron microscopy (STEM) imaging and energy-dispersive spectroscopy (EDS) measurements were performed at 300 kV on a FEI Titan Cube Themis G2 300 instrument equipped with a high-brightness field-emission gun (X-FEG), double spherical aberration corrector, and a monochromator. The cross-sectional STEM samples were fabricated by focused ion beam (FIB) cutting on FEI Helios NanoLab DualBeam 235.

4.4 Raman Spectroscopy Characterization.

Raman spectroscopy was performed at room temperature using two confocal Raman microscopes (LabRAM Odyssey and Jobin Yvon LabRAM HR800), with a 100× objective and 600 or 1800 lines/mm gratings. 532 nm and 633 nm lasers were used as the primary excitation source (spot size ~ 1 μm, actual laser power summarized in Table S4), without potential laser heating effects (Fig. S30). The Raman shift was calibrated using the characteristic phonon peak of silicon at 520.7 cm^{-1}. The linearly polarized and circularly polarized Raman spectra were collected by loading two half-wave plates and a quarter-wave plate. The detailed methods are shown in Fig. S12 and Supplementary Notes 6, 7. The temperature-dependent Raman spectroscopy was performed using in-situ thermal stages of KT-Z165M4LT (Zhengzhou Ketan Instrument Equipment Co., LTD.) with a 50× objective in vacuum.

4.5 He^+ Ion Irradiation Experiments.

Irradiation was performed using a Zeiss Orion NanoFab multi-ion beam system with a 30 keV He^+ beam. The ion dose σ was calculated as, $\sigma = NIt_0/Ae$, where I is ion current, t_0 is unit irradiation time (2 μs), N is the number of cycles, A is irradiated

Just Accepted

area, and e is the elementary charge. The dose was controlled from 0.01 to 200 ions/nm^2 by adjusting N and A.

Acknowledgements

The authors sincerely appreciate the valuable insights and professional guidance provided by Dr. Yang Teng and Dr. Liu Renhui. Their thoughtful opinions greatly helped us deepen our understanding and improve this paper. This work was financially supported by the National Natural Science Foundation of China (Nos. 52188101, 52122202, 52472052), the LiaoNing Revitalization Talents Program (Nos. XLYC2201003, XLYC2403170), and the National Key Research and Development Program of China (2023YFA1507002).

Electronic Supporting Information The Supporting Information is available free of charge at. Supporting Information included Optical images, AFM data, UV–vis absorption spectra, phonon dispersion calculations, polarized Raman analysis, He^+ irradiation supplementary spectra, and additional phonon mode tables and so on (Fig. S1–S29, Tables S1–S4 and Supplementary Note S1~S7) (PDF).

References

[1] Chang, C.; Chen, W.; Chen, Y.; Chen, Y.; Ding, F.; Fan, C.; Fan, H. J.; Fan, Z.; Gong, C.; Gong, Y. et al. Recent progress on two-dimensional materials. *Acta Phys. -Chim. Sin*. **2021**, *37*, 2108017.

[2] Ren, W.; Bøggild, P.; Redwing, J.; Novoselov, K. S.; Sun, L.; Qi, Y.; Jia, K.; Liu, Z.; Burton, O.; Alexander-Webber, J. et al. The 2D Materials roadmap. *2D Mater*. **2026**, *13*, 021501.

[3] Saito, R.; Tatsumi, Y.; Huang, S.; Ling, X.; Dresselhaus, M. S. Raman spectroscopy of transition metal dichalcogenides. *J. Phys.: Condens. Matter* **2016**, *28*, 353002.

Just Accepted

[4] Gao, X.; Zheng, L.; Luo, F.; Qian, J.; Wang, J.; Yan, M.; Wang, W.; Wu, Q.; Tang, J.; Cao, Y.; Tan, C.; Tang, J.; Zhu, M.; Wang, Y.; Li, Y.; Sun, L.; Gao, G.; Yin, J.; Lin, L.; Liu, Z.; Qin, S.; Peng, H. Integrated wafer-scale ultra-flat graphene by gradient surface energy modulation. *Nat. Commun*. **2022**, *13*, 5410.

[5] Ferrari, A. C.; Meyer, J. C.; Scardaci, V.; Casiraghi, C.; Lazzeri, M.; Mauri, F.; Piscanec, S.; Jiang, D.; Novoselov, K. S.; Roth, S.; Geim, A. K. Raman spectrum of graphene and graphene layers. *Phys. Rev. Lett*. **2006**, *97*, 187401.

[6] Lee, C.; Yan, H.; Brus, L. E.; Heinz, T. F.; Hone, J.; Ryu, S. Anomalous lattice vibrations of single- and few-layer MoS_2. *ACS Nano* **2010**, *4*, 2695-2700.

[7] Mignuzzi, S.; Pollard, A. J.; Bonini, N.; Brennan, B.; Gilmore, I. S.; Pimenta, M. A.; Richards, D.; Roy, D. Effect of disorder on Raman scattering of single-layer MoS_2. *Phys. Rev. B* **2015**, *91*, 195411.

[8] Lu, X.; Utama, M. I. B.; Lin, J.; Luo, X.; Zhao, Y.; Zhang, J.; Pantelides, S. T.; Zhou, W.; Quek, S. Y.; Xiong, Q. Rapid and nondestructive identification of polytypism and stacking sequences in few-layer molybdenum diselenide by raman spectroscopy. *Adv. Mater*. **2015**, *27*, 4502-4508.

[9] Zhang, Z.; Huang, Z.; Li, J.; Wang, D.; Lin, Y.; Yang, X.; Liu, H.; Liu, S.; Wang, Y.; Li, B.; Duan, X.; Duan, X. Endoepitaxial growth of monolayer mosaic heterostructures. *Nat. Nanotechnol*. **2022**, *17*, 493-499.

[10] Beams, R.; Cançado, L. G.; Novotny, L. Raman characterization of defects and dopants in graphene. *J. Phys.: Condens. Matter*. **2015**, *27*, 083002.

[11] Gontijo, R. N.; Bunker, N.; Graiser, S. L.; Ding, X.; Smeu, M.; Elías, A. L. Resonant Raman scattering study of strain and defects in chemical vapor deposition grown MoS_2 monolayers. *Small* **2024**, *21*, 2310685.

Just Accepted

[12] Zhao, Y.; Luo, X.; Li, H.; Zhang, J.; Araujo, P. T.; Gan, C. K.; Wu, J.; Zhang, H.; Quek, S. Y.; Dresselhaus, M. S.; Xiong, Q. Interlayer breathing and shear modes in few-trilayer MoS_2 and WSe_2. *Nano Lett*. **2013**, *13*, 1007-1015.

[13] Fang, S.; Duan, S.; Wang, X.; Chen, S.; Li, L.; Li, H.; Jiang, B.; Liu, C.; Wang, N.; Zhang, L.; Wen, X.; Yao, Y.; Zhang, J.; Xie, D.; Luo, Y.; Xu, W. Direct characterization of shear phonons in layered materials by Mechano-Raman spectroscopy. *Nat. Photonics* **2023**, *17*, 531-537.

[14] Wang, X.; Du, K.; Liu, Y. Y. F.; Hu, P.; Zhang, J.; Zhang, Q.; Owen, M. H. S.; Lu, X.; Gan, C. K.; Sengupta, P.; Kloc, C.; Xiong, Q. Raman spectroscopy of atomically thin two-dimensional magnetic iron phosphorus trisulfide ($FePS_3$) crystals. *2D Mater*. **2016**, *3*, 031009.

[15] He, C.; Xu, C.; Chen, C.; Tong, J.; Zhou, T.; Sun, S.; Liu, Z.; Cheng, H.-M.; Ren, W. Unusually high thermal conductivity in suspended monolayer $MoSi_2N_4$. *Nat. Commun*. **2024**, *15*, 4832.

[16] Hong, Y.-L.; Liu, Z.; Wang, L.; Zhou, T.; Ma, W.; Xu, C.; Feng, S.; Chen, L.; Chen, M.-L.; Sun, D.-M.; Chen, X.-Q.; Cheng, H.-M.; Ren, W. Chemical vapor deposition of layered two-dimensional $MoSi_2N_4$ materials. *Science* **2020**, *369*, 670-674.

[17] Liu, Z.; Wang, L.; Hong, Y.-L.; Chen, X.-Q.; Cheng, H.-M.; Ren, W. Two-dimensional superconducting $MoSi_2N_4(MoN)_{4n}$ homologous compounds. *Natl. Sci. Rev*. **2023**, *10*, nwac273.

[18] Mortazavi, B.; Javvaji, B.; Shojaei, F.; Rabczuk, T.; Shapeev, A. V.; Zhuang, X. Exceptional piezoelectricity, high thermal conductivity and stiffness and promising photocatalysis in two-dimensional $MoSi_2N_4$ family confirmed by first-principles. *Nano Energy* **2021**, *82*, 105716.

Just Accepted

[19] Deng, Z. Electric field enhancement effect on Raman spectra in two-dimensional $MoSi_2N_4$, $TiSi_2N_4$ and $MoGe_2As_4$ monolayers. *Solid State Commun*. **2022**, *358*, 114994.

[20] Oreshonkov, A. S.; Sukhanova, E. V.; Popov, Z. I. Phonon dynamics in $MoSi_2N_4$: insights from DFT calculations. *Phys. Chem. Chem. Phys.* **2023**, *25*, 29831-29841.

[21] Aroyo, M. I.; Kirov, A.; Capillas, C.; Perez-Mato, J. M.; Wondratschek, H. Bilbao Crystallographic Server. ii. representations of crystallographic point groups and space groups. *Acta Cryst.* **2006**, *A62*, 115-128.

[22] Aroyo, M. I.; Perez-Mato, J. M.; Orobengoa, D.; Tasci, E.; de la Flor, G.; Kirov, A. Crystallography online: Bilbao Crystallographic Server. *Bulg. Chem. Commun.* **2011**, *43*, 183-197.

[23] Carvalho, B. R.; Malard, L. M.; Alves, J. M.; Fantini, C.; Pimenta, M. A. Exciton-phonon coupling in 2D and bulk MoS_2 observed by resonance Raman scattering. *Phys. Rev. Lett*. **2015**, *114*, 136403.

[24] Huang, J.; Liu, Z.; Yang, T.; Zhang, Z. New selection rule of resonant Raman scattering in MoS_2 monolayer under circular polarization. *J. Mater. Sci. Technol*. **2022**, *102*, 132-136.

[25] Miller, B.; Lindlau, J.; Bommert, M.; Neumann, A.; Yamaguchi, H.; Holleitner, A.; Högele, A.; Wurstbauer, U. Tuning the Fröhlich exciton-phonon scattering in monolayer MoS_2. *Nat. Commun*. **2019**, *10*, 807.

[26] Yang, D.-Y.; Li, M.; Sun, L.; Zhou, T.; Tong, J.; Chen, C.; Zhao, W.; Liu, X.; Wang, H.; Zhao, L.; Li, H.; Li, H.; Liu, Z.; Li, X.; Qin, S.; Zhu, M.; Xu, C.; Ren, W. Wafer-scale and doping-tunable p-Type semiconducting monolayer WSi_2N_4 film. *Natl. Sci. Rev*. **2026**, nwag191.

Just Accepted

[27] Li, H.; Zhang, Q.; Yap, C. C. R.; Tay, B. K.; Edwin, T. H. T.; Olivier, A.; Baillargeat, D. From bulk to monolayer MoS_2: evolution of Raman scattering. *Adv. Funct. Mater*. **2012**, *22*, 1385-1390.

[28] Song, Q. J.; Tan, Q. H.; Zhang, X.; Wu, J. B.; Sheng, B. W.; Wan, Y.; Wang, X. Q.; Dai, L.; Tan, P. Physical origin of Davydov splitting and resonant Raman spectroscopy of Davydov components in multilayer $MoTe_2$. *Phys. Rev. B* **2016**, *93*, 115409.

[29] He, C. CVD growth, optical, and thermal properties of 3R-phase WSi_2N_4 and $MoSi_2N_4$. Ph.D. Dissertation, University of Science and Technology of China, Shenyang, China, **2025**.

[30] Wang, X.; Lin, J.; Zhu, Y.; Luo, C.; Suenaga, K.; Cai, C.; Xie, L. Chemical vapor deposition of trigonal prismatic NbS_2 monolayers and 3R-polytype few-layers. *Nanoscale* **2017**, *9*, 16607-16611.

[31] Reich, S.; Ferrari, A. C.; Arenal, R.; Loiseau, A.; Bello, I.; Robertson, J. Resonant Raman scattering in cubic and hexagonal boron nitride. *Phys. Rev. B* **2005**, *71*, 205201.

[32] del Corro, E.; Terrones, H.; Elias, A.; Fantini, C.; Feng, S.; Nguyen, M. A.; Mallouk, T. E.; Terrones, M.; Pimenta, M. A. Excited excitonic states in 1L, 2L, 3L, and bulk WSe_2 observed by resonant Raman spectroscopy. *ACS Nano* **2014**, *8*, 9629-9635.

[33] Kim, S.; Kim, K.; Lee, J.-U.; Cheong, H. Excitonic resonance effects and Davydov splitting in circularly polarized Raman spectra of few-layer WSe_2. *2D Mater*. **2017**, *4*, 045002.

[34] Na, W.; Kim, K.; Lee, J.-U.; Cheong, H. Davydov splitting and polytypism in few-layer MoS_2. *2D Mater*. **2019**, *6*, 015004.

Just Accepted

[35] Nguyen, M. H.; Park, G.; Park, J.-G.; Cheong, H. Interlayer interaction and Davydov splitting in antiferromagnetic few-layer $NiPS_3$. *npj Quantum Mater*. **2025**, *10*, 65.

[36] Rabelo, C.; Vasconcelos, T. L.; Archanjo, B. S.; Cançado, L. G.; Jorio, A. Micro- and nano-Raman spectroscopy characterization of exfoliated graphene with helium-ion microscope patterned line defects. *Phys. Status Solidi B* **2023**, *260*, 2300204.

[37] Pimenta, M. A.; del Corro, E.; Carvalho, B. R.; Fantini, C.; Malard, L. M. Comparative study of Raman spectroscopy in graphene and MoS_2-type transition metal dichalcogenides. *Acc. Chem. Res.* **2015**, *48*, 41−47.

[38] Wang, Q.; Cao, L.; Liang, S.-J.; Wu, W.; Wang, G.; Lee, C. H.; Ong, W. L.; Yang, H. Y.; Ang, L. K.; Yang, S. A.; Ang, Y. S. Efficient ohmic contacts and built-in atomic sublayer protection in $MoSi_2N_4$ and WSi_2N_4 monolayers. *npj 2D Mater. Appl*. **2021**, *5*, 71.

[39] Ma, H.; Zhao, W.; Zhang, Q.; Liu, D.; Ren, H.; Zhu, H.; Chi, Y.; Ding, F.; Guo, W. Chemical environment dependent stabilities, electronic properties and diffusions behaviors of intrinsic point defects in novel two-dimensional $MoSi_2N_4$ Monolayer. *Appl. Surf. Sci*. **2022**, *592*, 153214.

[40] Hafner, J. Materials simulations using VASP—a quantum perspective to materials science. *Comput. Phys. Commun*. **2007**, *177*, 6-13.

[41] Kohn, W.; Sham, L. J. Self-consistent equations including exchange and correlation effects. *Phys. Rev*. **1965**, *140*, A1133-A1138.

[42] Blöchl, P. E. Projector augmented-wave method. *Phys. Rev. B* **1994**, *50*, 17953-17979.

[43] Perdew, J. P.; Burke, K.; Ernzerhof, M. Generalized gradient approximation made simple. *Phys. Rev. Lett*. **1996**, *77*, 3865-3868.

Just Accepted

[44] Kresse, G.; Furthmüller, J. Efficient iterative schemes for ab initio total-energy calculations using a plane-wave basis set. *Phys. Rev. B* **1996**, *54*, 11169-11186.

[45] Grimme, S.; Antony, J.; Ehrlich, S.; Krieg, H. A consistent and accurate ab initio parametrization of density functional dispersion correction (DFT-D) for the 94 elements H–Pu. *J. Chem. Phys*. **2010**, *132*, 154104.

[46] Wang V.; Xu N.; Liu J. C.; Tang G.; Geng W. T. VASPKIT: A User-Friendly Interface Facilitating High-Throughput Computing and Analysis Using VASP Code. *Comput. Phys. Commun*. **2021**, *267*, 108033.

[47] Togo, A. First-principles phonon calculations with Phonopy and Phono3py. *J. Phys. Soc. Jpn.* **2023**, *92*, 012001.

[48] Skelton, J. M.; Burton, L. A.; Jackson, A. J.; Oba, F.; Parker, S. C.; Walsh, A. Lattice dynamics of the tin sulphides SnS_2, SnS and Sn_2S_3: vibrational spectra and thermal transport. *Phys. Chem. Chem. Phys*. **2017**, *19*, 12452-12465.

Just Accepted

Electronic Supplementary Material

Raman spectra of van der Waals layered $MoSi_2N_4$ and WSi_2N_4

Chen Chen[1,2], Dayong Yang[1,2], Xiaoqiao Hu[1,2], Yan Liang [1], Chuan Xu[1,2], and Wencai Ren[1,2]**

[1]Shenyang National Laboratory for Materials Science, Institute of Metal Research, Chinese Academy of Sciences, Shenyang 110016, China

[2]School of Materials Science and Engineering, University of Science and Technology of China, Shenyang 110016, China

*Address correspondence to Wencai Ren, wcren@imr.ac.cn; Chuan Xu, xuc@imr.ac.cn

Supporting information to https://doi.org/10.26599/NR.2026.94909269

The supplementary information includes:

Fig. S1-30

Supplementary Note 1~7

Table S1-4

Just Accepted

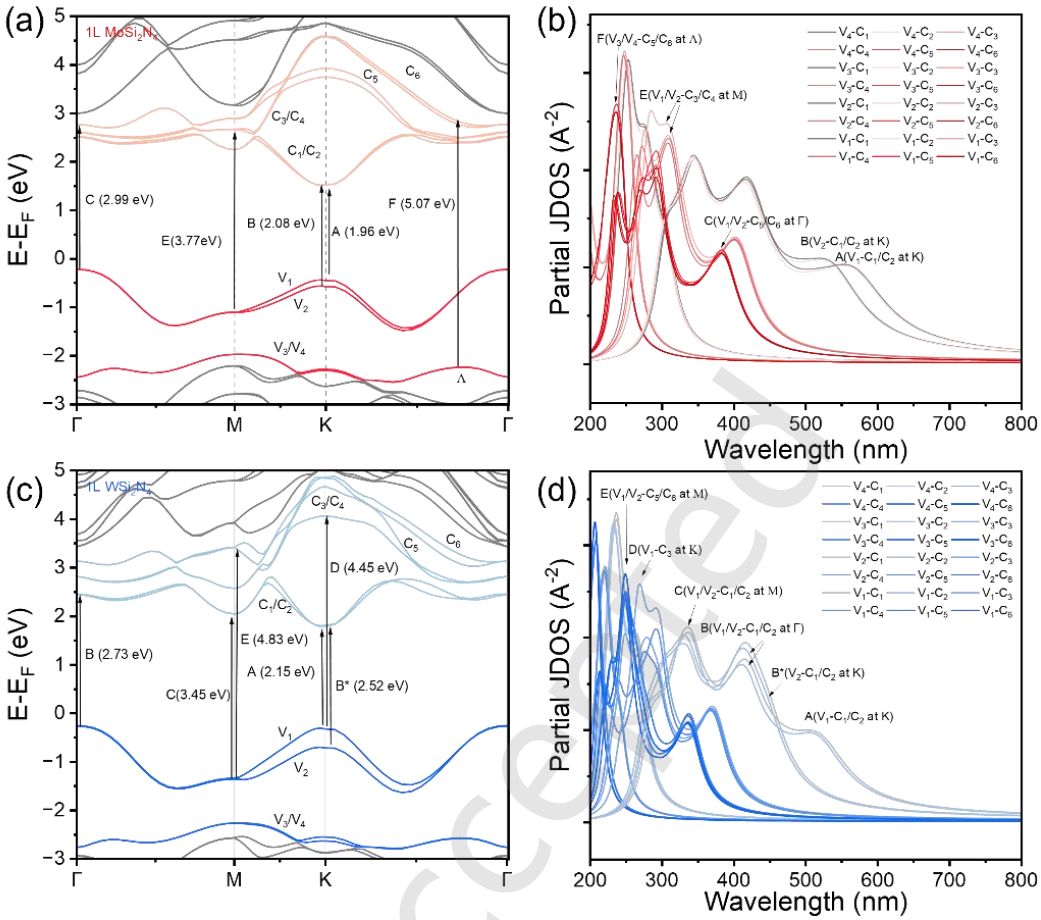


Fig. S1. Electronic band structures and partial joint density of states (JDOS) of 1L $MoSi_2N_4$ (a, b) and WSi_2N_4 (c,d).

Just Accepted

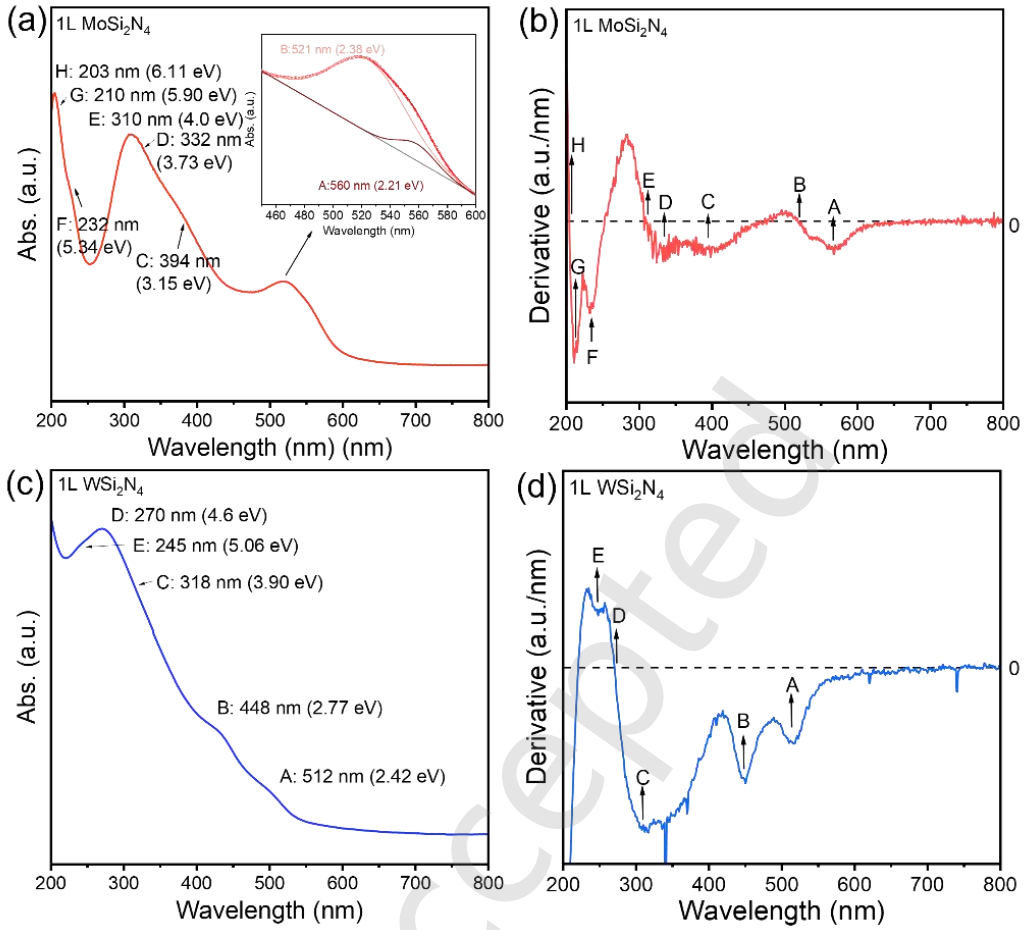


Fig. S2. UV-vis optical absorption spectra and derivative spectra of 1L $MoSi_2N_4$ (a, b) and WSi_2N_4 (c, d) films. For ease of comparison, an offset of 0.26 eV and 0.27 eV was applied to (b) and (d), respectively.

Just Accepted

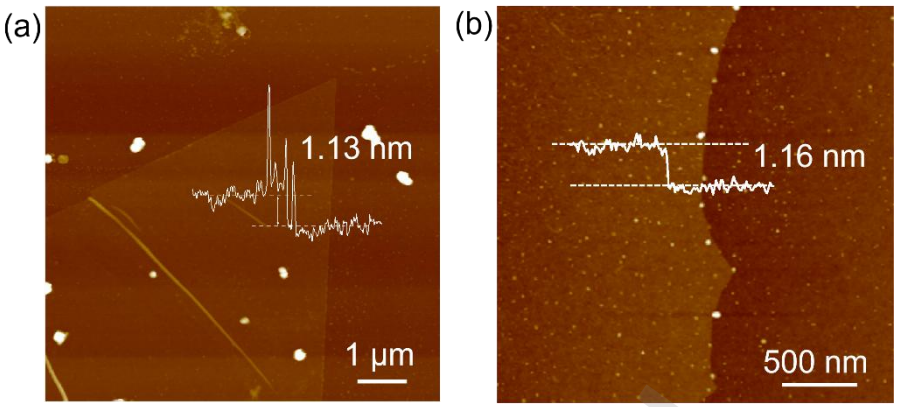


Fig. S3. Atomic force microscopy (AFM) images of 1L $MoSi_2N_4$ with a thickness of ~1.13 nm (a) and 1L WSi_2N_4 with a thickness of ~1.16 nm (b).

Just Accepted

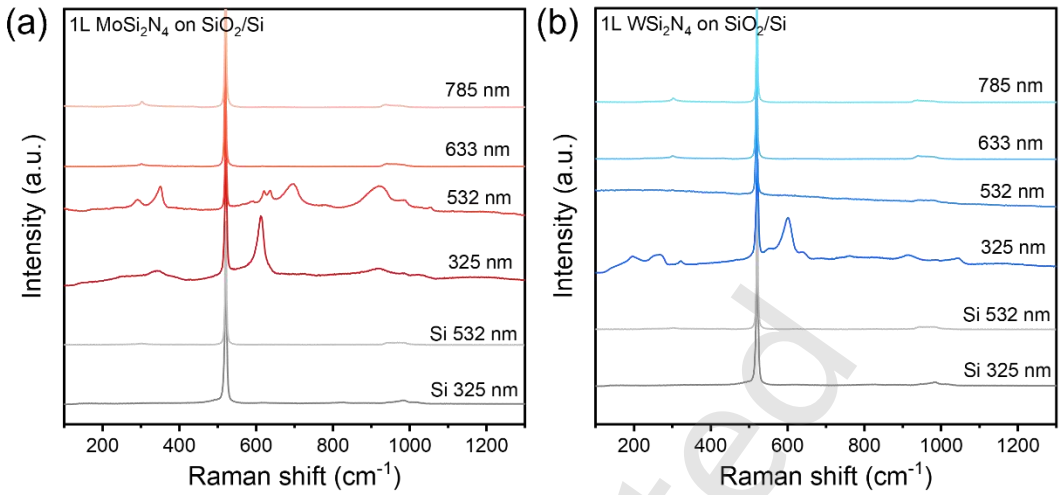


Fig. S4. Raman spectra of (a) 1L $MoSi_2N_4$ and (b) 1L WSi_2N_4 under different excitation wavelengths (325 nm, 532 nm, 633 nm, and 785 nm).

Just Accepted

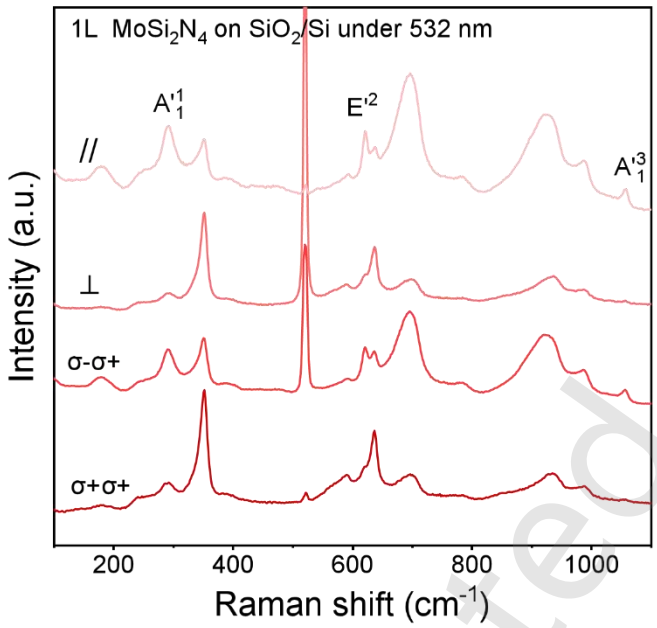


Fig. S5. Linearly and circularly polarized Raman spectra of 1L $MoSi_2N_4$ under 532 nm. Under exciton resonance, the Fröhlich interaction renders the Raman tensor forms of A and E modes identical [1], so that polarization measurements cannot reliably separate first- and second-order features, nor discriminate between E' and A'_1 symmetries.

Just Accepted

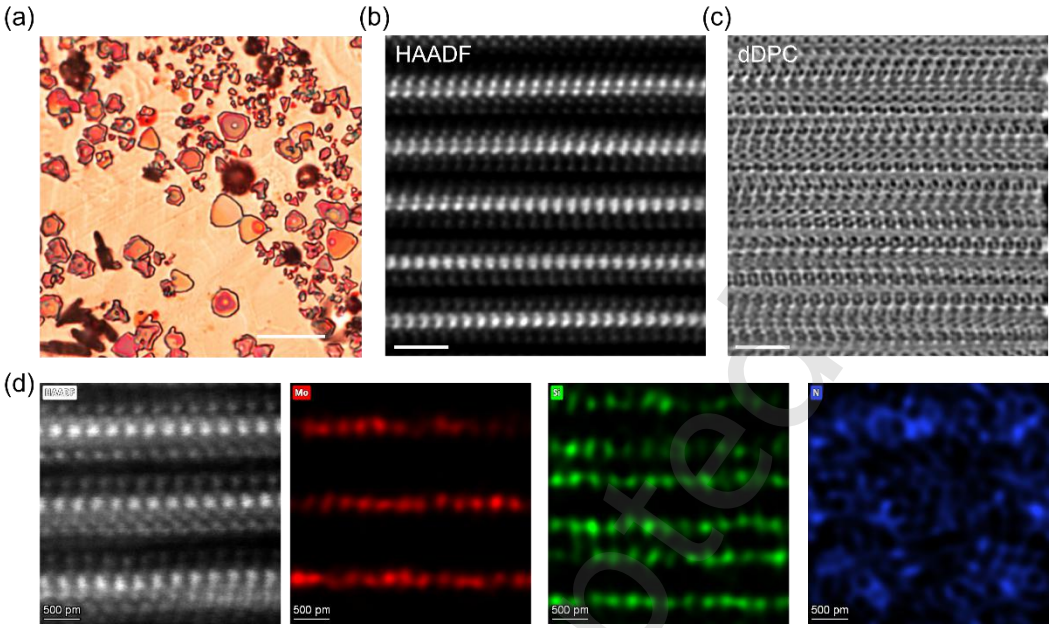


Fig. S6. Structural characterization of as-grown 3R-phase $MoSi_2N_4$ crystals. (a) Optical image of the as-grown 3R-phase $MoSi_2N_4$ crystals on Cu/Mo substrates. Scale bars: 10 μm. (b, c) Cross-sectional STEM images of 3R-phase $MoSi_2N_4$: (b) HAADF and (c) dDPC. (d) EDS mapping of 3R-phase $MoSi_2N_4$, confirming the seven-atomic-layer structure (N-Si-N-Mo-N-Si-N) of a monolayer.

Just Accepted

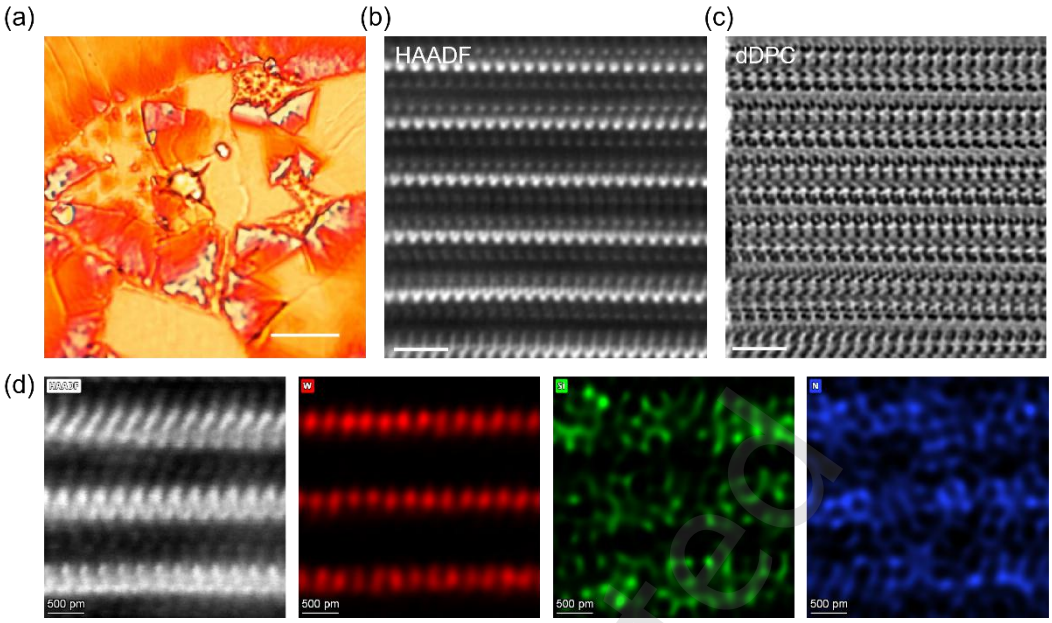


Fig. S7. Structural characterization of as-grown 3R-phase WSi_2N_4 crystals. (a) Optical image of the as-grown 3R-phase WSi_2N_4 crystals on Cu/W substrates. Scale bars: 10 μm. (b, c) Cross-sectional STEM images of 3R-phase WSi_2N_4: (b) HAADF and (c) dDPC. (d) EDS mapping of 3R-phase WSi_2N_4, confirming the seven-atomic-layer structure (N-Si-N-W-N-Si-N) of a monolayer.

Just Accepted

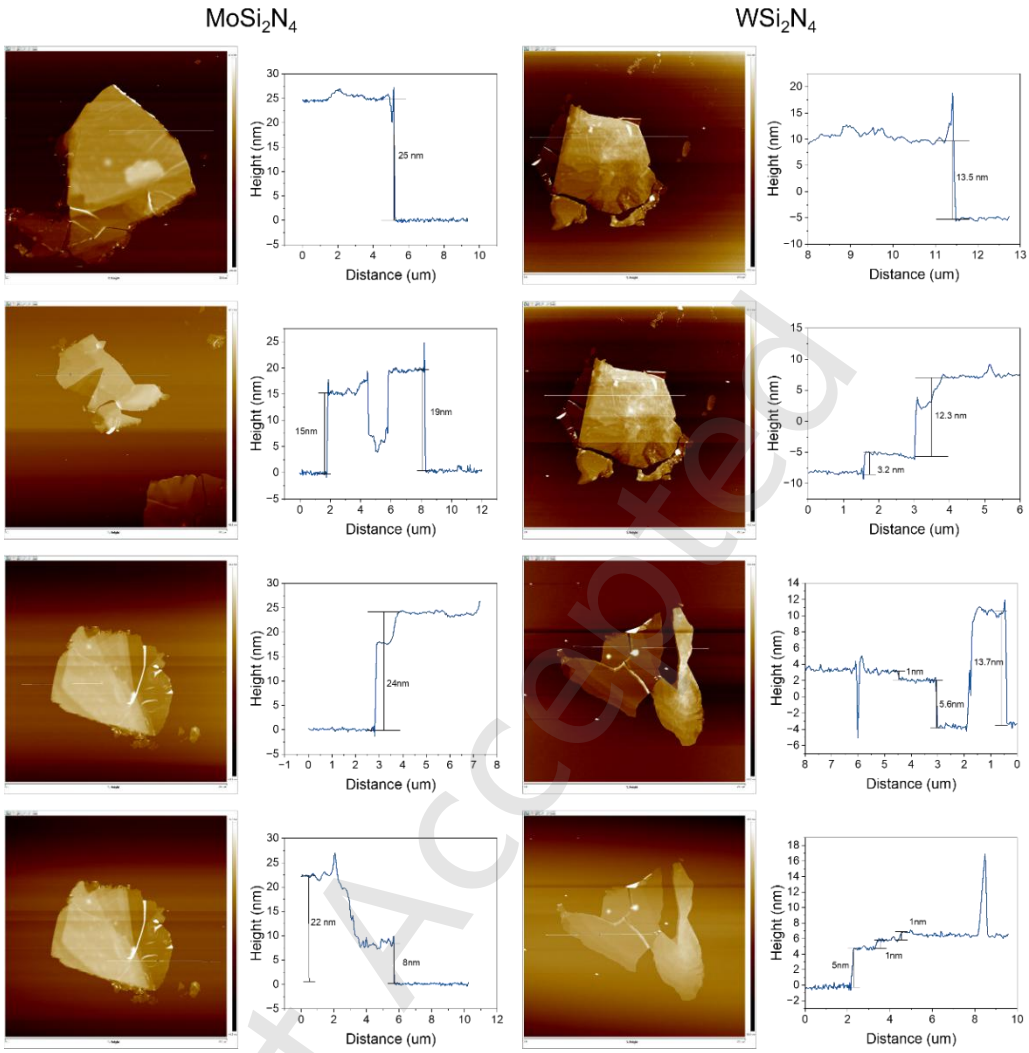


Fig. S8. AFM characterization of $MoSi_2N_4$ and WSi_2N_4 crystals. Topography images of $MoSi_2N_4$ or WSi_2N_4 flakes with varying layer thicknesses transferred onto SiO_2/Si substrates.

Just Accepted

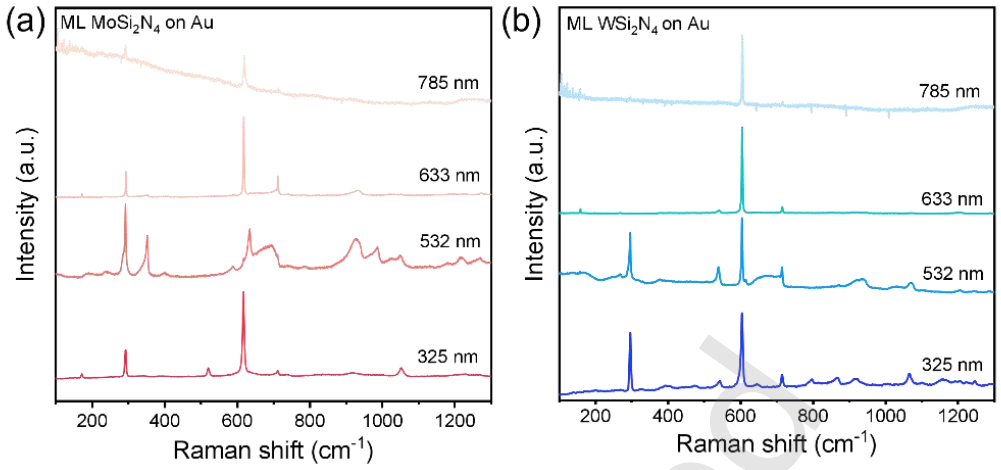


Fig. S9. Raman spectra of ML $MoSi_2N_4$ (a) and ML WSi_2N_4 (b) under different excitation wavelengths (325 nm, 532 nm, 633 nm, and 785 nm).

Just Accepted

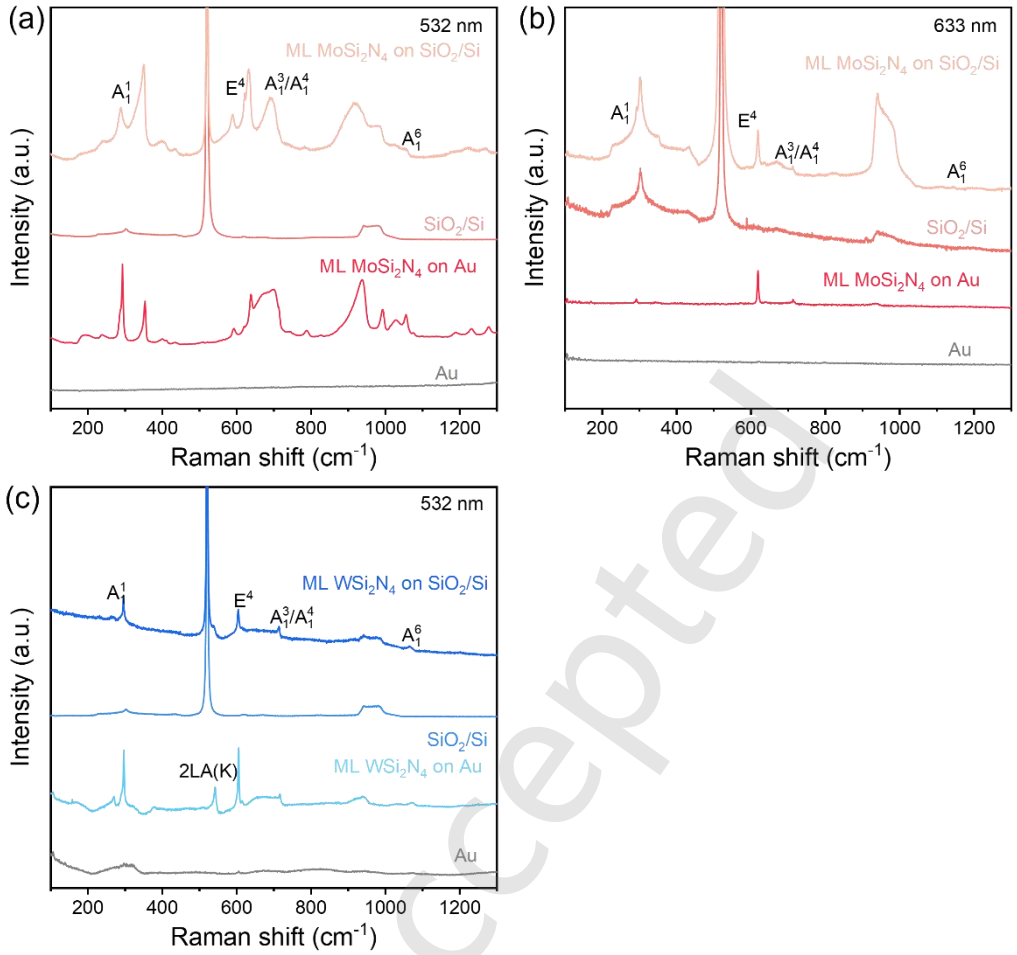


Fig. S10. Comparative Raman spectra of multilayer $MoSi_2N_4$ (532 nm (a), 633 nm (b)) and WSi_2N_4 (532 nm (c)) on Au and SiO_2/Si substrates, including the bare Au reference. The intensity differences between the two substrates are attributed to variations in layer number. The spectra highlight the strong interfering signal from the SiO_2/Si substrate versus the much weaker background on Au under non-resonant excitation.

Just Accepted

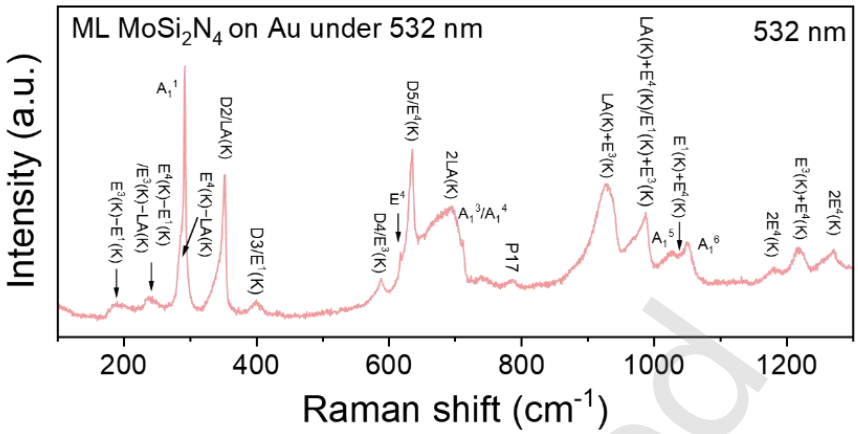


Fig. S11. Raman spectrum of ML $MoSi_2N_4$ grown on an Au substrate, measured under 532 nm laser excitation.

Just Accepted

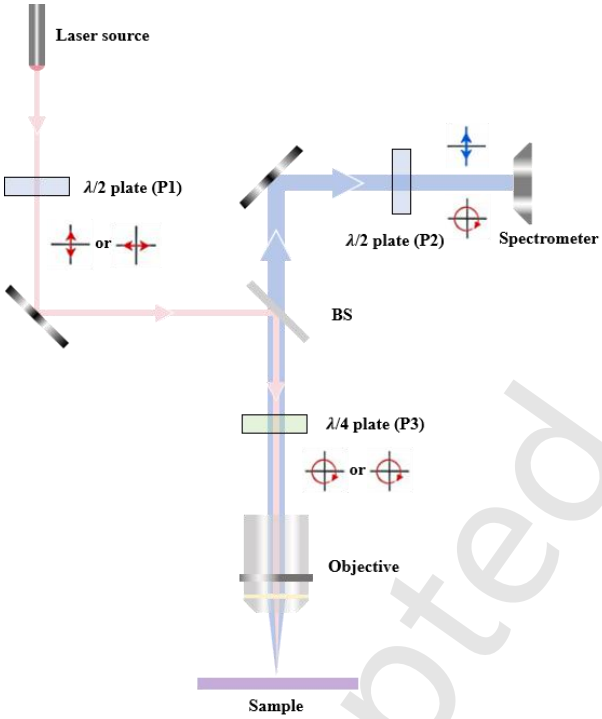


Fig. S12. Schematic of the experimental setup for angle-resolved polarization Raman spectroscopy.

Just Accepted

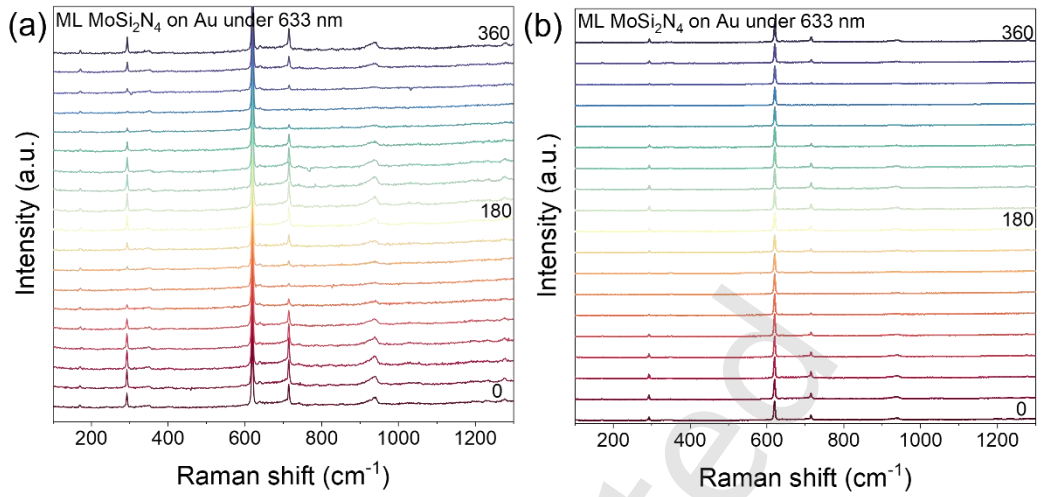


Fig. S13. Angle-resolved polarization Raman spectra of ML $MoSi_2N_4$ on a SiO_2/Si substrate, acquired under 633 nm laser excitation.

Just Accepted

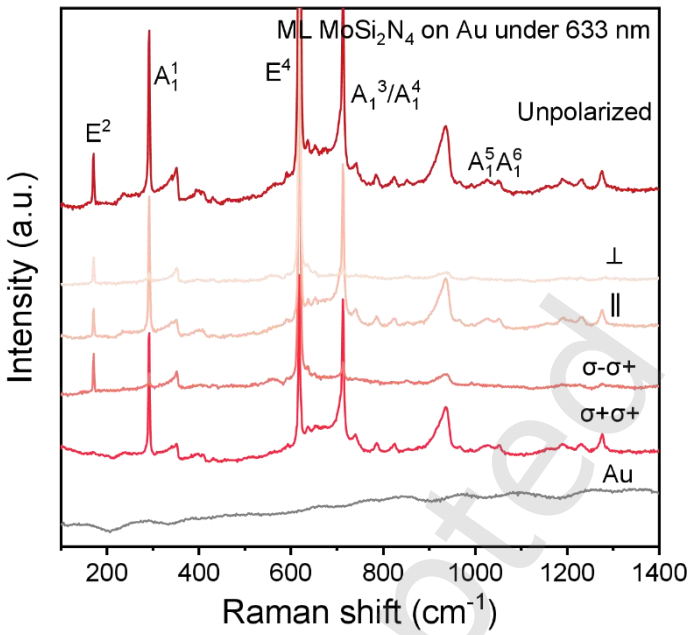


Fig. S14. Linearly and circularly polarized Raman spectra of ML $MoSi_2N_4$ on a SiO_2/Si substrate, acquired under 633 nm laser excitation.

Just Accepted

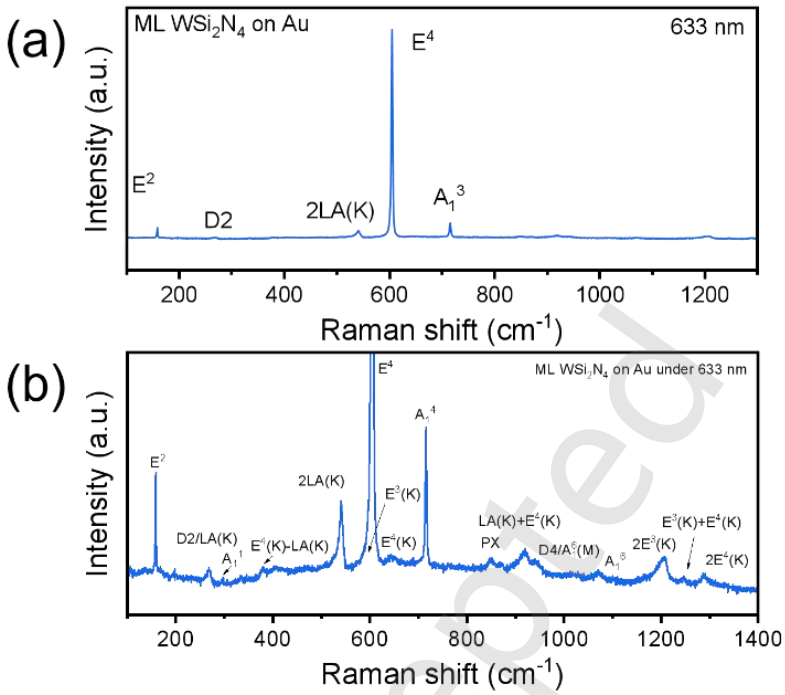


Fig. S15. Raman spectrum of ML WSi_2N_4 grown on an Au substrate, measured under 633 nm laser excitation.

Just Accepted

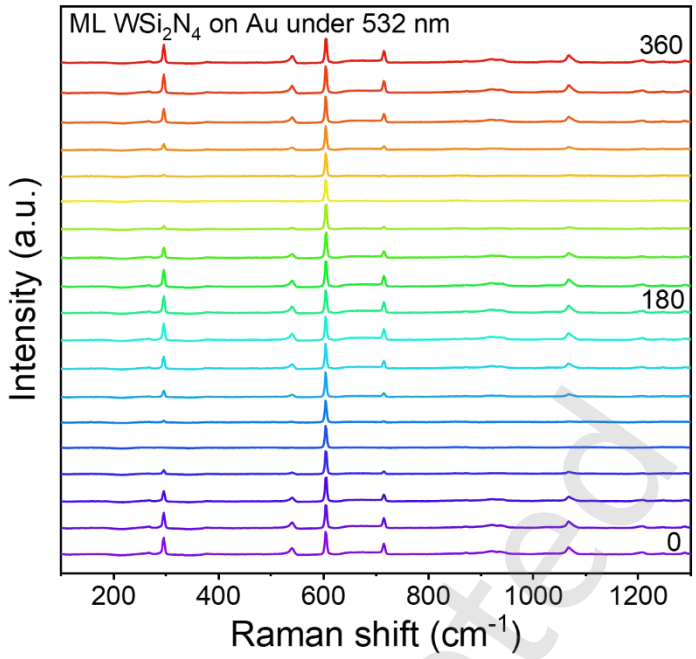


Fig. S16. Angle-resolved polarization Raman spectra of ML WSi_2N_4 on a SiO_2/Si substrate, acquired under 532 nm laser excitation.

Just Accepted

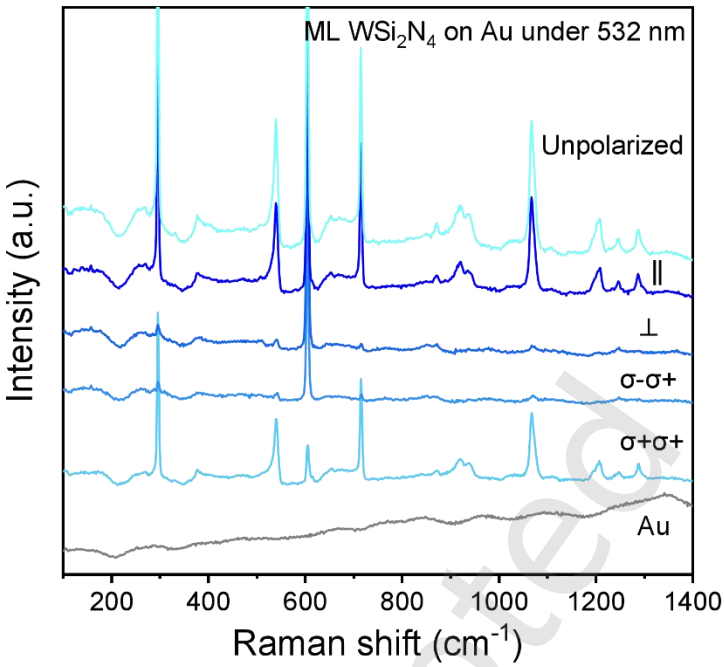


Fig. S17. Linearly and circularly polarized Raman spectra of ML WSi_2N_4 on a SiO_2/Si substrate, acquired under 532 nm laser excitation.

Just Accepted

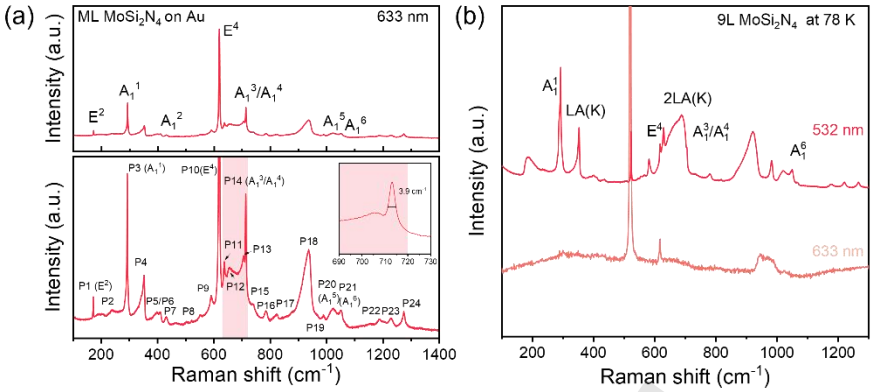


Fig. S18. (a) Raman spectrum of ML $MoSi_2N_4$ under 633 nm excitation. The inset shows the Full- width at half- maximum (FWHM) of the A_1^4 mode. (b) Raman spectra of 9L $MoSi_2N_4$ at 78 K under 532 nm and 633 nm.

Just Accepted

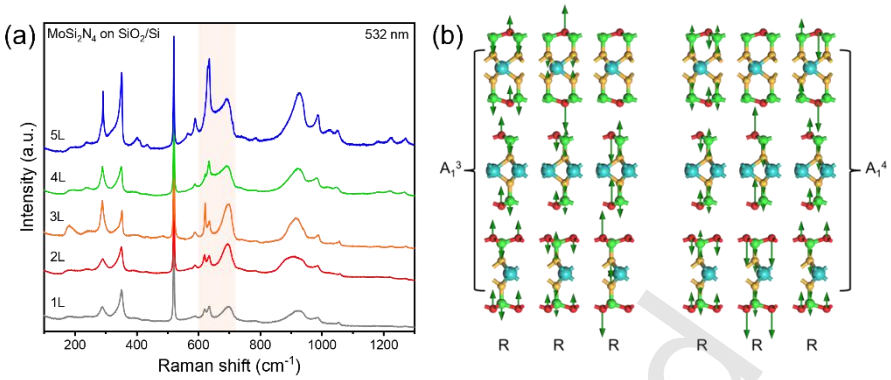


Fig. S19. (a) Raman spectra of 1-5 layer $MoSi_2N_4$ on a SiO_2/Si substrate, acquired under 532 nm laser excitation. (b) Vibrational patterns of the A_1^3 and A_1^4 modes of 3R-phase MSi_2N_4 (M = Mo, W).

Under resonance- enhanced conditions, the 2LA(K) peak of monolayer $MoSi_2N_4$ exhibits a symmetric line shape. With increasing layer number, the linewidth broadens and the peak becomes asymmetric, similar to the 2D peak in graphene [2].

Just Accepted

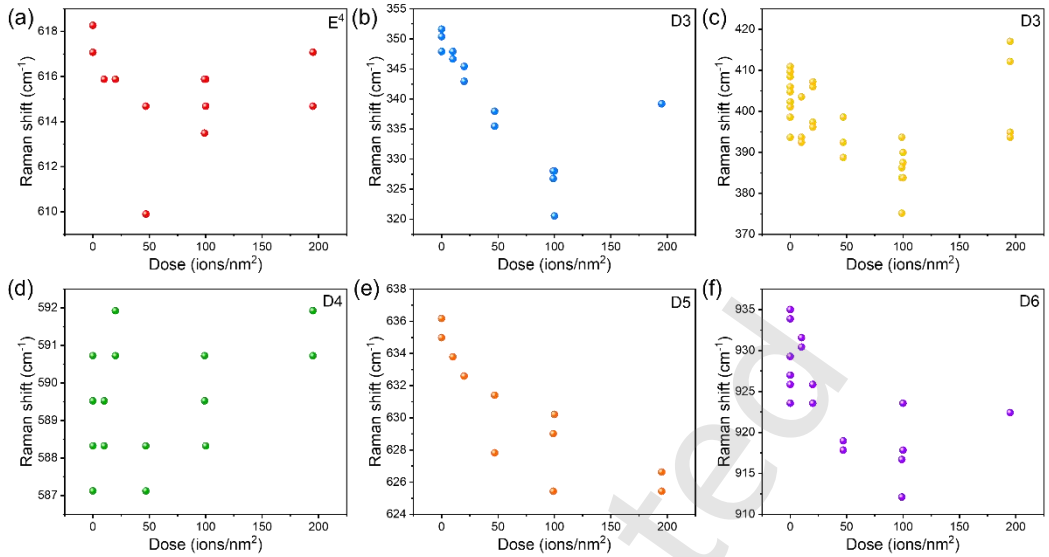


Fig. S20. Shift of Raman peak positions in ML $MoSi_2N_4$ as a function of irradiation dose.

Just Accepted

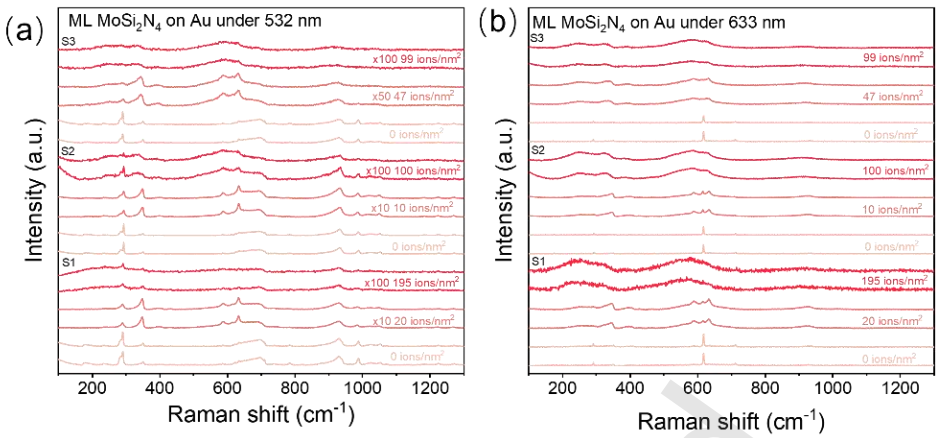


Fig. S21. Evolution of Raman spectra of ML $MoSi_2N_4$ with irradiation dose under 532 nm (a) and 633 nm excitation (b).

Just Accepted

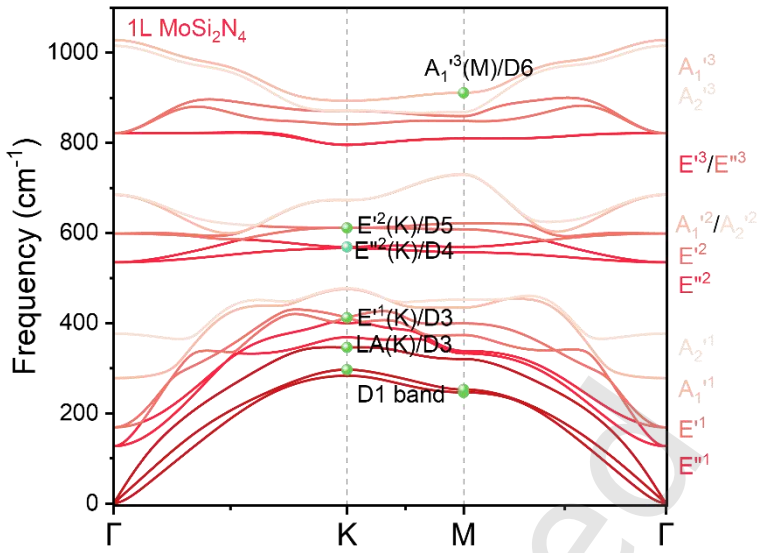


Fig. S22. Phonon dispersion curves of 1L $MoSi_2N_4$, with defect-activated phonon branches indicated.

Just Accepted

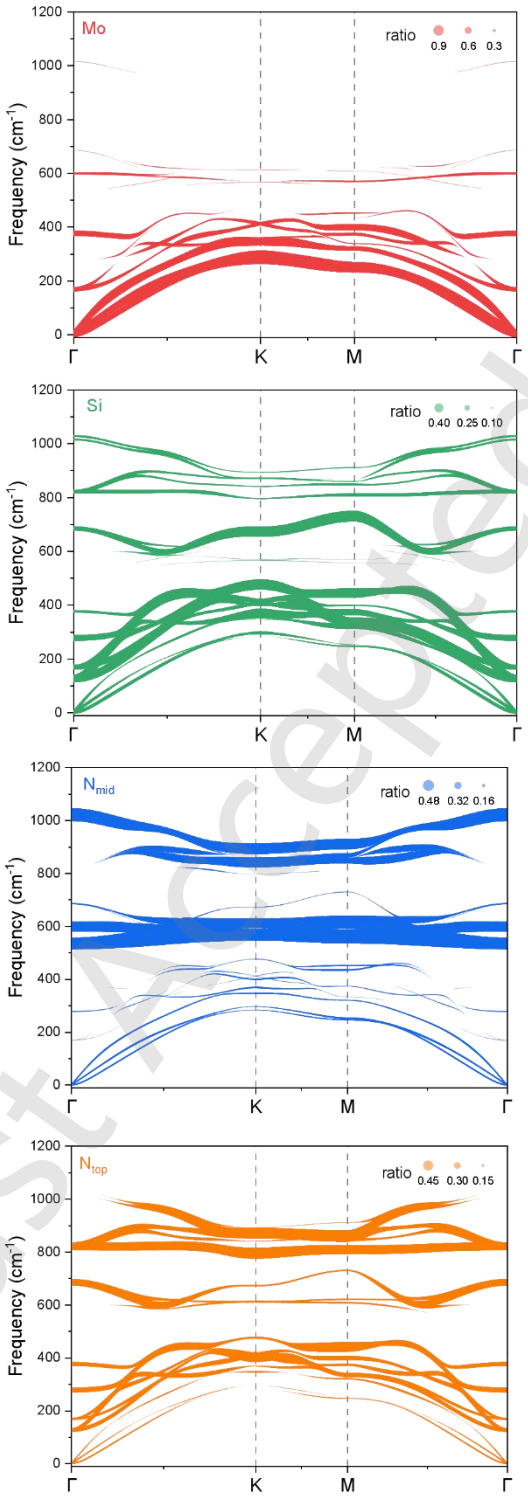


Fig. S23. Element-projected phonon dispersion curves of 1L $MoSi_2N_4$.

Just Accepted

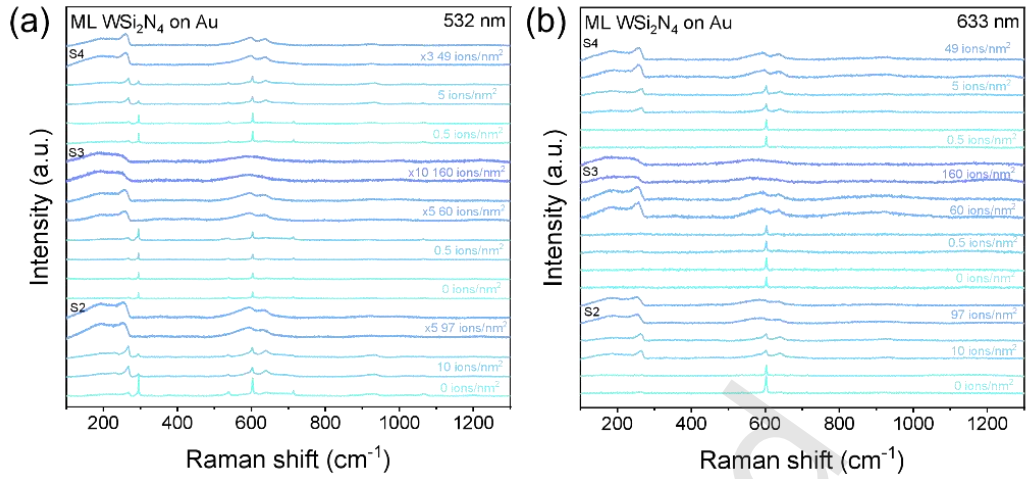


Fig. S24. Evolution of Raman spectra of ML WSi_2N_4 with irradiation dose under 532 nm (a) and 633 nm excitation (b).

Just Accepted

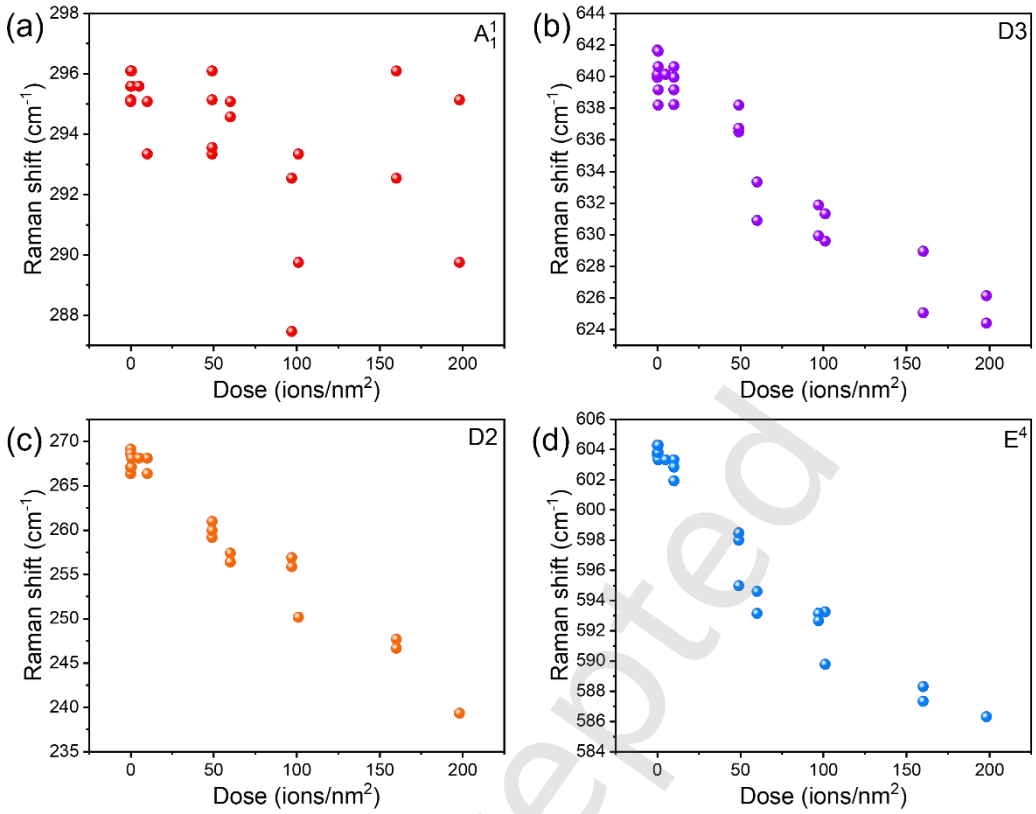


Fig. S25. Shift of Raman peak positions in ML WSi_2N_4 as a function of irradiation dose, acquired under 633 nm laser excitation.

Just Accepted

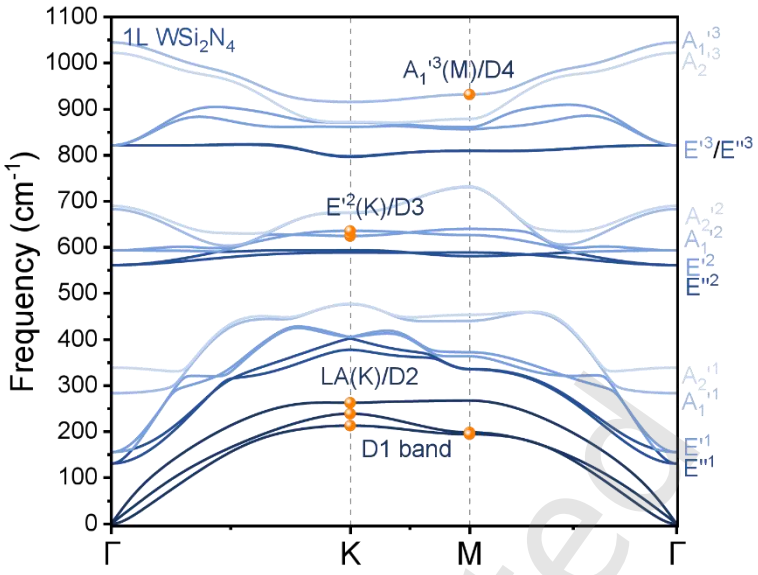


Fig. S26. Phonon dispersion curves of 1L WSi_2N_4, with defect-activated phonon branches indicated.

Just Accepted

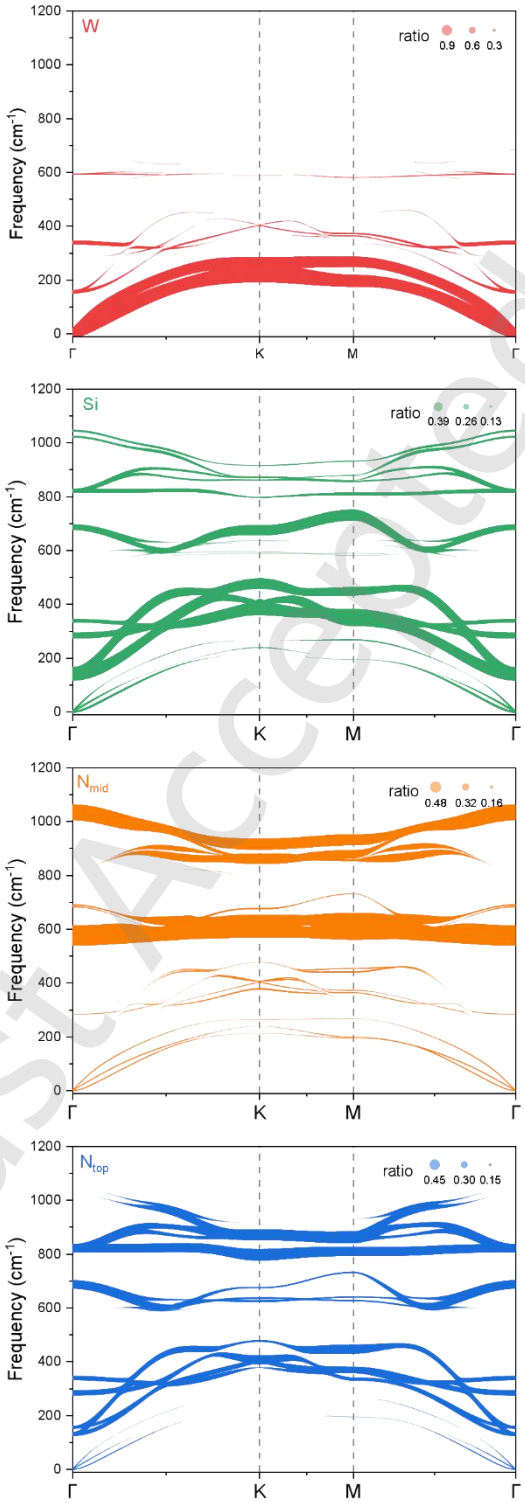
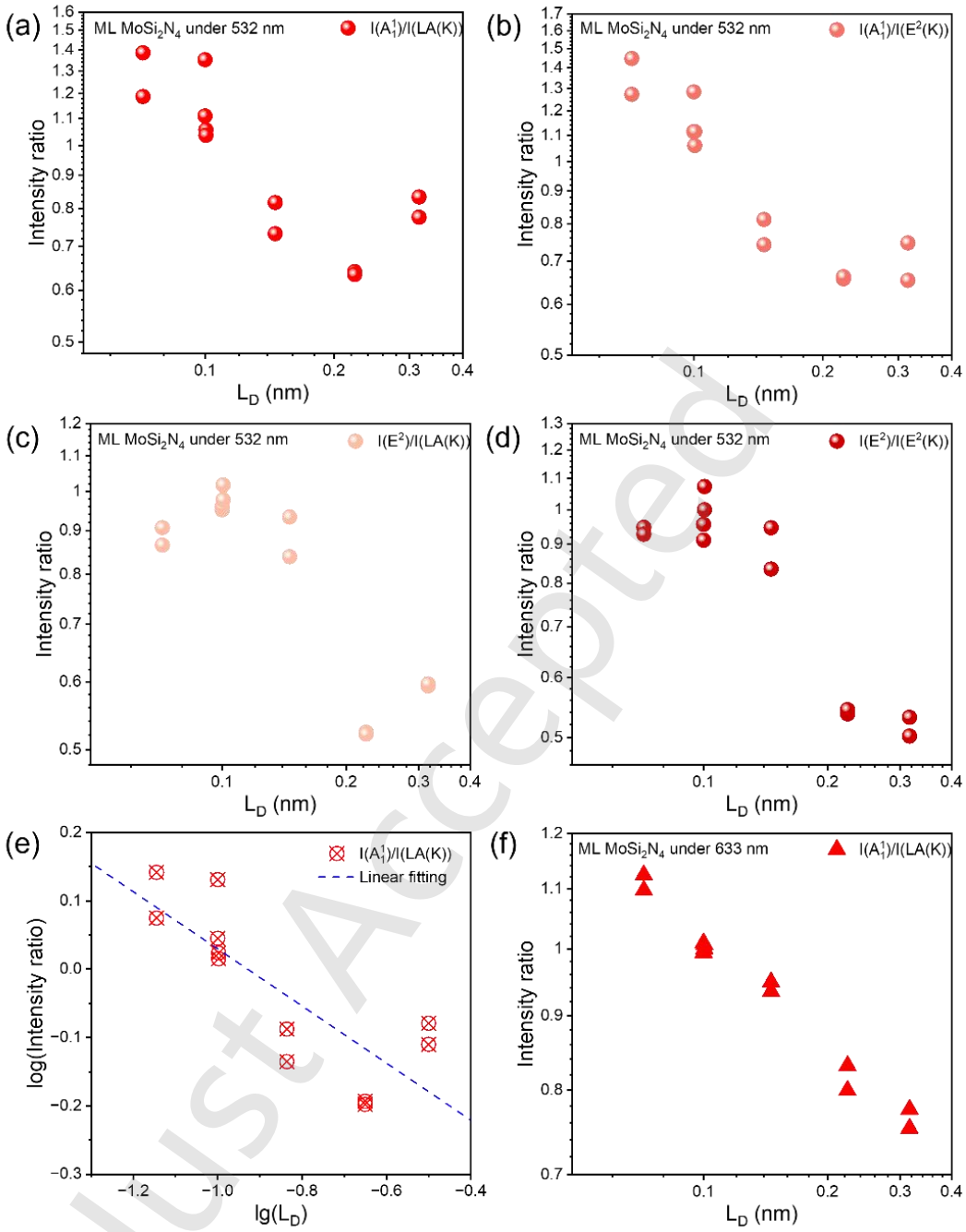


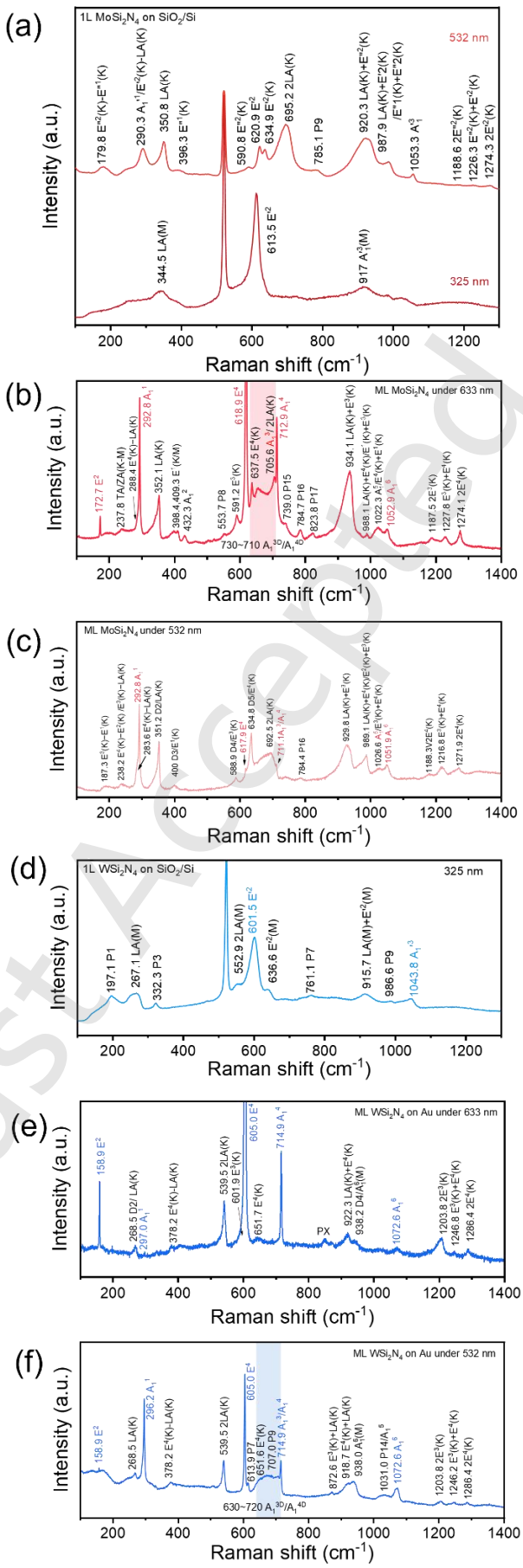
Fig. S27. Element-projected phonon dispersion curves of 1L WSi_2N_4.

Just Accepted



Just Accepted

Fig. S28. The relationship between I_X/I_D and the defect concentration. (a~d) Intensity ratios of A_1^1/LA(K) (a), A_1^1/E^4(K) (b), E^4/LA(K) (c), and E^4/E^4(K) (d) in the 532 nm excitation spectra plotted against defect concentration. (e) Linear fitting of the logarithmic function of L_D versus I_X/I_D, revealing an approximately linear relationship. (f) Intensity ratios of A_1^1/LA(K) in the 633 nm excitation spectra plotted against defect concentration.



Just Accepted

Fig. S29 Preliminary Raman peak assignments for monolayer and multilayer MSi_2N_4 (M = Mo, W) under different excitation wavelengths. (a) Raman spectra of 1L $MoSi_2N_4$ under 325 nm and 532 nm laser excitation. (b, c) Raman spectra of ML $MoSi_2N_4$ under 633 nm (b) and 532 nm (c) excitation. (d) Raman spectrum of 1L WSi_2N_4 under 325 nm laser excitation. (e, f) Raman spectra of ML WSi_2N_4 under 633 nm (e) and 532 nm (f) excitation. Preliminary assignments for most observed Raman peaks are provided.

Just Accepted

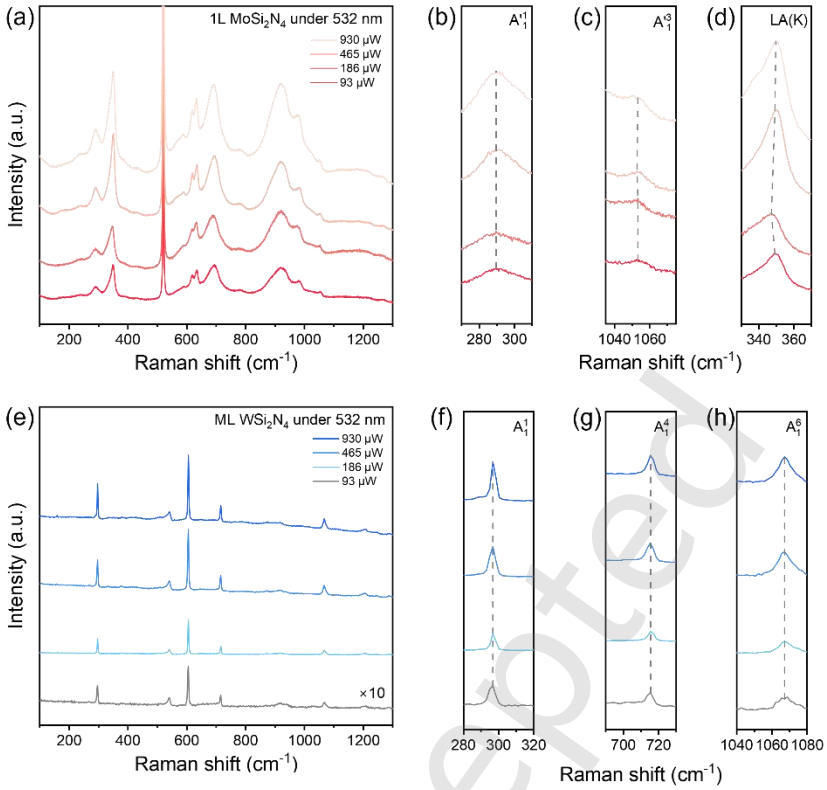


Fig. S30 Laser heating effect on Raman spectra of 1L $MoSi_2N_4$ and ML WSi_2N_4 under 532 nm. (a) Power-dependent Raman spectra of 1L $MoSi_2N_4$. (b~d) $A_1'^1$ (b), $A_1'^3$ (c) and LA(K) (d) Raman peak evolutions extracted from (a). (e) Power-dependent Raman spectra of ML WSi_2N_4. (f~h) A_1^1 (f), A_1^4 (g) and A_1^6 (h) Raman peak evolutions extracted from (e).

Just Accepted

Just Accepted

Supplementary Note 1. Theoretical analysis of Raman activity and polarization selectivity of 1L and 3R phase MSi_2N_4

Table S1: Character Table of Point Group D_{3h} and C_{3v}

D_{3h}		C_{3v}	
Mult.	Quadratic	Mult.	Quadratic
A'_1	x^2+y^2, z^2	A_1	x^2+y^2, z^2
A'_2	\	A_2	\
A''_1	\	E	x^2-y^2, xy
A''_2	z		
E'	x^2-y^2, xy		
E''	xz, yz		

According to Raman selection rules, the intensity of Raman scattering is governed by the Raman tensor R, the polarization vector of incident light e_s, and the polarization vector of scattered light e_i. This relationship can be expressed as:

$$I \propto |e_s \cdot R \cdot e_i|^2 \#(1-1)$$

Under non- resonant conditions, the Raman tensors for 1L and 3R- phase MSi_2N_4 take the following forms (based on their point groups):

For 1L MSi_2N_4

$$R_{A'_1} = \begin{pmatrix} a & 0 & 0 \\ 0 & a & 0 \\ 0 & 0 & b \end{pmatrix}$$

$$R_{E'} = \begin{pmatrix} c & 0 & 0 \\ 0 & -c & 0 \\ 0 & 0 & 0 \end{pmatrix}, \begin{pmatrix} 0 & -c & 0 \\ -c & 0 & 0 \\ 0 & 0 & 0 \end{pmatrix}$$

$$R_{E''} = \begin{pmatrix} 0 & 0 & 0 \\ 0 & 0 & d \\ 0 & d & 0 \end{pmatrix}, \begin{pmatrix} 0 & 0 & 0 \\ 0 & d & 0 \\ 0 & 0 & -d \end{pmatrix} \#(1-2)$$

For 3R phase MSi_2N_4

$$R_{A_1} = \begin{pmatrix} e & 0 & 0 \\ 0 & e & 0 \\ 0 & 0 & f \end{pmatrix}$$

Just Accepted

$$R_E = \begin{pmatrix} 0 & g & h \\ g & 0 & 0 \\ h & 0 & 0 \end{pmatrix}, \begin{pmatrix} g & 0 & 0 \\ 0 & -g & h \\ 0 & h & 0 \end{pmatrix} \#(1-3)$$

Here, a~h denote the nonzero Raman tensor elements. For linearly polarized light propagating along the out- of- plane direction, e_s and e_i can be written as $(\cos\omega, \sin\omega, 0)$ denotes the polarization angle θ relative to a crystallographic axis c. By combining Equations (1-1), (1-2) and (1-3), the polarization-dependent Raman intensity for the A'$_1$, E', and E'' modes in 1L and A_1 and E modes in 3R-phase MSi_2N_4 can be derived as a function of the polarization angle θ:

For 1L MSi_2N_4

$$I_{A_1'} = |a|^2 \sin^4\theta + |b|^2 \cos^4\theta + \frac{1}{2}|a||b| \sin^2(2\theta)\, cos\varphi_{ab} \#(1-4)$$

$$I_{E'} = c^2 \#(1-5)$$

$$I_{E''} = 0 \#(1-6)$$

For 3R-phase MSi_2N_4

$$I_{A_1} = |e|^2 \sin^4\theta + |f|^2 \cos^4\theta + \frac{1}{2}|e||f| \sin^2(2\theta)\, cos\varphi_{ab} \#(1-7)$$

$$I_E = g^2 \#(1-8)$$

For circularly polarized light propagating along the crystal's out- of- plane direction, e_s and e_i can be written as $\frac{1}{\sqrt{2}}(1, \pm i, 0)$.

For 1L MSi_2N_4 under co-circular polarization (σ+σ+)

$$I_{A_1'} = \left|\frac{1}{2}(a + i \cdot ia)\right|^2 = 0 \#(1-9)$$

Just Accepted

$$I_E = \left|\frac{1}{2}(c + i \cdot - ic)\right|^2 = c^2 \#(1-10)$$

For 1L MSi_2N_4 under cross-circular polarization (σ-σ+)

$$I_{A'_1} = \left|\frac{1}{2}(a - i \cdot ia)\right|^2 = a^2 \#(1-11)$$

$$I_E = \left|\frac{1}{2}(c - i \cdot - ic)\right|^2 = 0 \#(1-12)$$

For 3R-phase MSi_2N_4 under co-circular polarization (σ+σ+)

$$I_{A_1} = \left|\frac{1}{2}(e + i \cdot ie)\right|^2 = 0 \#(1-13)$$

$$I_E = g^2 \#(1-14)$$

For 3R-phase MSi_2N_4 under cross-circular polarization (σ-σ+)

$$I_{A_1} = \left|\frac{1}{2}(e - i \cdot ie)\right|^2 = e^2 \#(1-15)$$

$$I_E = 0 \#(1-16)$$

Just Accepted

Supplementary Note 2. Analysis of UV-vis absorption spectra of monolayer $MoSi_2N_4$ and WSi_2N_4

To extract absorption peaks, we adopted a combined analysis of UV-vis absorption spectra and their first derivatives [3]. Among them, the zero- crossing point (changing from positive to negative) is used to identify the main absorption peak, and the minimum value of the first- order derivative is used to identify the shoulder peak. Specifically, for $MoSi_2N_4$, there are three zero- points and five minima located at 2.21, 2.38, 3.15, 3.73, 4.0, 5.34, 5.90, 6.11 eV (Fig. S2a, b), labeled A to H in sequence, respectively. Similarly, for WSi_2N_4, we extracted five absorption peaks A, B, C, D and E located at 2.42, 2.77, 3.90, 4.6 and 5.06 eV (Fig. S2c, d), respectively.

The joint density of states (JDOS) quantifies the number of available electronic transitions at a given photon energy, thus serving as a fundamental tool for analyzing optical absorption [4]. Furthermore, the partial JDOS further restricts the analysis to specific pairs of valence and conduction bands, thereby enabling the assignment of observed peaks to particular interband transitions.

Fig. S1a and S1c show the band structures of monolayer $MoSi_2N_4$ and WSi_2N_4. Here, we selected four valence bands (V_1~V_4) and six conduction bands (C_1~C_6) closest to the Fermi level to calculate partial JDOS (Fig. S1b, d). Because of the strong spin-orbit coupling (SOC) from the heavy Mo atoms, the top of the valence band at the K point splits into two bands, V_1 and V_2. For monolayer $MoSi_2N_4$, the absorption spectrum in Fig. S1a exhibits eight peaks, including A (2.21 eV), B (2.38 eV), C (3.15 eV), D (3.73 eV), E (4.0 eV), F (5.34 eV), G (5.90 eV) and H (6.11 eV). To facilitate a direct comparison between the JDOS and the absorption spectrum, an offset of 0.26 eV was applied to the data presented in Fig. S1b. The transitions are assigned as follows: peak A corresponds to transitions from V_1 to C_1/C_2 at K corresponding to 2.24 eV, peak B from V_2 to C_1/C_2 at K corresponding to 2.32 eV, and peak C from V_1/V_2 to C_5/C_6 at Γ corresponding to 3.25 eV, and peak E from V_1/V_2 to C_5/C_6 at M corresponding to 4.03 eV. Peak F mainly originates from transitions from the deeper valence bands V_3/V_4 to C_5/C_6 near the Λ point corresponding to 5.33 eV. Peak H could not be assigned within the selected energy window, likely involving multiple higher-energy transition pathways. The D and G peaks are excluded from the

Just Accepted

peak assignment analysis owing to their negligible intensities, and no corresponding electronic transitions for these peaks could be resolved in the partial JDOS and band structure.

For monolayer WSi_2N_4, the absorption spectrum in Fig. S1c clearly resolves five peaks A (2.42 eV), B (2.77 eV), C (3.90 eV), D (4.6 eV), and E (5.06 eV). An offset of 0.27 eV was applied to the data presented in Fig. S1d. Similar to $MoSi_2N_4$, the valence band at K is split by SOC effect, but the split V_2 band does not exhibit a significant transition probability at K (B* in Fig. S1d). Accordingly, peak A corresponds to transitions from V_1 to C_1/C_2 at K (2.42 eV), and peak B corresponds to transitions from V_1/V_2 to C_1/C_2 at Γ (3.0 eV). Peak C mainly originates from transitions from V_1/V_2 to C_1/C_2 at M (3.72 eV). Peak D mainly originates from transitions from V_1 to C_3/C_4 at K (4.72 eV). Peak E mainly originates from transitions from V_1/V_2 to C_5/C_6 at K (5.09 eV). Notably, although the B* peak (V_2 to C_1/C_2 at K) is predicted at 2.52 eV in the band structure, it is absent in the partial JDOS (2.79 eV).

Just Accepted

Table S2: The theoretically calculated and experimentally measured Raman peak positions of $MoSi_2N_4$ (Unit: cm^{-1})

1L $MoSi_2N_4$			3R phase $MoSi_2N_4$		
Mode/Lab.	Cal.	Exp. (532 nm)	Mode/Lab.	Cal.	Exp. (633 nm)
E''^1	126.8		E^1	127.5	
E'^1	168.5		E^2(P1)	168.7	172.7
E''^2(K)-E''^1(K)/E (P1)		179.8			
			ZA(K/M)/TA(K/M) (D1)	246-293	237.8-295.4
			E^4(K)−E^2(K) /E^3(K)−LA(K) (P2)		239.1
			A_1^{1D}	275.6	
$A_1'^1$ (P2)	277.7	290.3	A_1^1 (P3)	278.2	292.8
LA (K) (P3)	345.9	350.8	LA(K) (P4/D2)	332.2	352.1
E''^1(K) (P4)	412.1	396.3	E^1 (K-M) (P5+P6/D3)	368.2	398.4,409.3
$A''_2{}^1$	376.4		A_1^2/A_1^{2D}	377.5	
			P7		432.3
E'^2	534.6		E^3	535.0	
			P8		553.7
E''^2(K) (P5)	568.8	590.8	E^3(K) (P9/D4)	568.8	591.2
E''^2 (P6)	598.6	620.9	E^4 (P10)	599.0	618.9
E'^2(K) (P7)	611.1	634.9	E^4(K) (P11/D5)	604.3	637.2
			A_1^{3D} (P12)	637.6	654.0
			A_1^3 A_1^4 Davydov	637.6-694.9	630-710
$A'_1{}^2$	685.4		A_1^3/A_1^{4D}	685.7/686.8	
2LA(K) (P8)		695.2	2LA(K) (P13)		705.1
$A''_2{}^2$	685.9		A_1^4 (P14)	694.9	712.9
			P15		739.0
P9		785.1	P16		784.7
E'^3/E''^3	821.1		E^5/E^6	822.1/822.6	
			P17		823.8
			D6 (A_1^6(M))	910.9	927.0
LA(K)+E''^2(K) (P10)		920.3	LA(K)+E^3(K) (P18)		930-936
LA(K)+E'^2(K) /E''^1(K)+E''^2(K) (P11)		987.9	LA(K)+E^4(K) /E^2(K)+E^3(K) (P19)		988.1
			A_1^{5D}	990.1	
$A''_2{}^3$	1015.0		A_1^5 (P20)	1023.7	1025.6
$A'_1{}^3$ (P12)	1027.9	1053.3	A_1^6/A_1^{6D} (P21)	1028.6	1052.9
2E''^2(K) (P13)		1188.6	2E^3(K) (P22)		1187.5
E''^2(K)+E'^2(K) (P14)		1226.3	E^3(K)+ E^4(K) (P23)		1227.8
2E'^2(K) (P15)		1274.3	2E^4(K) (P24)		1274.1

Just Accepted

Table S3: The theoretically calculated and experimentally measured Raman peak positions of WSi_2N_4 (Unit: cm^{-1}).

1L WSi_2N_4			3R phase WSi_2N_4		
Mode/Lab.	Cal.	Exp. (325 nm)	Mode/Lab.	Cal.	Exp. (532 nm)
E''^1	130.6		E^1	131	
E'^1	155.4		E^2 (P1)	155.0	158.9
P1		195.6	ZA/TA(M-K) (D1 band)	194-246	189.3-242.3
LA(M) (P2)	267.1	267.1	LA(K) (P2/D2)	255.2	268.5
			A_1^{1D}	281.5	
$A'_1{}^1$	283.2		A_1^1 (P3)	282.9	296.2
P3		322.3	A_1^{2D}	336.8	
$A''_2{}^1$	338.8		A_1^2	337.8	
			E^4(K)-LA(K) (P4)		378.2
2LA(M) (P4)		552.9	2LA(K) (P5)		539.5
E''^2	561.2		E^3	552.2	
			E3(K)	588.4	604.5
E'^2 (P5)	593.0	601.5	E^4 (P6)	583.6	605.0
			P7		613.9
E'^2(M) (P6)	624, 635	636.6	E^4(K) (D3)	624.5	634.8
			A_1^3/A_1^4 Davydov	633-690	630-720
			A_1^{3D} (P8)	633.4	651.6
$A'_1{}^2$	682.9		A_1^3	687.0	
			A_1^{4D}	687.5	
			P9		707.0
$A''_2{}^2$	689.8		A_1^4 (P10)	690.4	714.9
P7		761.1			
E'^3	821.0		E^5	818.6	
E'^3	821.2		E^6	819.2	
			E^3(K)+LA(K) (P11)		872.7
$A'_1{}^3$(M)		915.7	LA(K)+E^4(K) (P12)		918.7
LA(K)+E''^2(K)(P8)			A_1^6(M) (D4)	931.7	922.3
			P13		938.2
P9		986.6	A_1^{5D}	987.7	
$A''_2{}^3$	1022.1		A_1^5 (P14)	1027.2	1031.0
$A'_1{}^3$ (P10)	1044.6	1043.8	A_1^6/A_1^{6D} (P15)	1039.7	1072.6
			$2E^3$(K) (P16)		1203.8
			E^3(K)+E^4(K) (P17)		1246.8
			$2E^4$(K) (P18)		1286.4

Just Accepted

Table S4: Measured actual laser power below the objective lens under different wavelengths (Unit: μW)

Wavelength	LabRAM Odyssey		Jobin Yvon LabRAM HR800	
	50×	100×	50×	100×
532 nm	246	186	166	120
633 nm	288	260	299	259
785 nm	1190	805	\	\

The actual laser powers below the objective lens were measured by a laser power meter (PM160, THORLABS GmbH, wavelength range: 400–1100 nm) for the 532 nm, 633 nm, and 785 nm lasers. The 325 nm laser exceeds the power meter's detection range and therefore cannot be measured. The actual laser power fluctuates within a range of ±10%.

Just Accepted

Supplementary Note 3. Preliminary identification of second-order Raman peaks in MSi_2N_4

The first-order Raman peaks and defect-activated peaks have been analyzed and assigned in the main text, providing a reference for identifying overtone modes (2X) and combination modes (X1 ± X2), whose scattering processes correspond to scenarios (ii) and (iv) in Fig. 1(e), respectively. In ML $MoSi_2N_4$, the defect-activated peaks D2 (LA(K), P4, 352.1 cm^{-1}), D3 (E^1(K), P5/P6, 398.4/409.2 cm^{-1}), D4 (E^3(K), P9, 591.2 cm^{-1}), and D5 (E^4(K), P11, 637.2 cm^{-1}) are attributed to phonon–defect scattering. Their corresponding overtone modes, phonon-phonon scattering, are assigned to P9 (705.1 cm^{-1}), P22 (1187.5 cm^{-1}), and P24 (1274.1 cm^{-1}) in Fig. S29 (b, c), respectively. Consequently, P9, P22, and P24 are tentatively assigned as 2LA(K), 2E^3(K), and 2E^4(K), respectively. The corresponding combination modes are identified as P18 (930-936 cm^{-1}, LA(K) + E^3(K)), P19 (988.1 cm^{-1}, LA(K) + E^4(K)/E^1(K) + E^3(K)), and P23 (1227.8 cm^{-1}, E^3(K) + E^4(K)). The corresponding difference modes are E^4(K) - E^1(K)/E^3(K) - LA(K) (239.1 cm^{-1}), E^3(K) - E^1(K) (178.9 cm^{-1}) in Fig. S11. The E^4(K) - LA(K) and the E^4(K) + E^2(K) modes overlap with the A_1^1, A_1^5 and A_1^6 modes, while the E^3(K) - E^4(K) mode lies outside the measured spectral range. Furthermore, D6 peak (A_1^6(M) 927.0 cm^{-1}) overlaps with P18 (930-936 cm^{-1}, LA(K) + E^3(K)).

Based on the Raman spectra of ML samples, the Raman peaks of 1L $MoSi_2N_4$ can be fully identified (Fig. 2 (e)). P3, P4, P5, and P7 are defect peaks in Fig. S29 (a), LA(K), E'^{1}(K), E"^{2}(K), and E'^{2}(K), respectively. P8, P13 and P15 are the overtone peaks of P3, P5 and P7, namely 2LA(K), 2E'^{2}(K) and 2E"^{2}(K). P10, P11 and P14 are combination peaks, LA(K) + E"^{2}(K), LA(K) + E'^{2}(K)/E"^{1}(K) + E"^{2}(K) and E'^{2}(K) + E"^{2}(K), respectively. P1 is the difference mode E"^{2}(K) - E"^{1}(K).

The 325 nm excitation energy is close to the M-point electronic transition energy of $MoSi_2N_4$, thus enhancing Raman scattering near the M point at this wavelength. Therefore, P3(341.4 cm^{-1}) and P10 (918.7 cm^{-1}) under the 325 nm excitation are preliminarily assigned to the LA(M) (320.2 cm^{-1}) and A'$_1^3$(M) (910.9 cm^{-1}) modes

Just Accepted

(Fig. S29a), respectively, whose frequencies are close to those of LA(K) and $A'_1{}^3$(K) in Fig. S22.

In ML WSi_2N_4, the defect-activated peaks D2 (LA(K), P4, 268.5 cm^{-1}), D3 (E^4(K), 634.8 cm^{-1}) and D4 ($A_1{}^6$(M), 922.3 cm^{-1}) are identified. Their corresponding overtone modes are assigned to P5 (2LA(K), 539.5 cm^{-1}) and P18 ($2E^4$(K), 1286.4 cm^{-1}) in Fig. S29 (e, f), respectively. By analogy with $MoSi_2N_4$, P16 (1203.8 cm^{-1}) and P17 (1246.8 cm^{-1}) are attributed to $2E^3$(K) and E^3(K) + E^4(K), respectively, although their parent defect peak E^3(K) overlaps with E^4 (P6, 605.0 cm^{-1}). Further identification of combination and difference modes yields P12 (E^4(K) + LA(K), 918.7 cm^{-1}), P4 (E^4(K) - LA(K), 378.2 cm^{-1}), and P11 (E^3(K) + LA(K), 872.7 cm^{-1}). The difference mode E^3(K) - LA(K) (expected at 337.8 cm^{-1}) is not observed. By contrast, this mode can be observed in the 1L WSi_2N_4 spectrum. Based on the above analysis, the Raman peaks of the 1L WSi_2N_4 are identified (Fig. 2f and S29d). Due to the alignment of the 325 nm laser with the energy level of the M-point transition, the second-order scattering process is more likely to occur at the M-point. P2, P4, P6 and P8 are tentatively assigned as LA(M) (267.1 cm^{-1}), 2LA(M) (552.9 cm^{-1}), E'^2(M) (636.6 cm^{-1}) and $A'_1{}^3$(M) (915.7 cm^{-1}). The corresponding assignments are summarized in Tables S2,3 and Fig. S29.

Just Accepted

Supplementary Note 4. Abnormal Davydov splitting behavior

The low-frequency breathing modes are the low-frequency manifestation of interlayer van der Waals forces, and the Davydov splitting modes are the high-frequency manifestation of interlayer van der Waals forces. The relationship between them is as follows [5]:

$$\omega_{Dai}^2=\omega_0^2+\omega_{LB_i}^2 \#(2-1)$$

Among them, ω_{Da_i}, ω_0, and ω_{LB_i} are the frequency of the Davydov splitting peak A_i, the frequency of the lowest Davydov splitting peak, and the frequency of the low-frequency breathing mode LB_i, respectively. Combined with the LCM model [6],

$$\omega_{LB_i}=\sqrt{\frac{K}{2\mu\pi^2c^2}[1\text{-}cos(\frac{i\text{-}1}{N}\pi)]} \#(2-2)$$

Among them, μ is the mass per unit area, c is the speed of light, N is the number of layers, and K is the interlayer interaction force constant. Equation 2-3 can be derived from equations 2-1 and 2-2

$$\omega_{Da_i}^2\text{-}\omega_{Da_j}^2=\left(\omega_{Da_i}+\omega_{Da_j}\right)\left(\omega_{Da_i}\text{-}\omega_{Da_j}\right)$$

$$=\frac{K}{2\mu\pi^2c^2}[cos\left(\frac{j\text{-}1}{N}\pi\right)\text{-}cos(\frac{i\text{-}1}{N}\pi)] \#(2-3)$$

From equations (2-3), for a given sample thickness, the bandwidth of the Davydov splitting peaks in the high-frequency A_1 mode is predicted to be narrower than that of the low-frequency ones.

Our first-principles calculations of the $MoSi_2N_4$ phonon dispersion curves revealed that specific A_1 modes undergo exceptionally large Davydov splitting (Fig. 3d, e). Calculated splitting widths for the A_1^1, A_1^2, A_1^3, A_1^4, A_1^5, and A_1^6 modes are 2.5, 0.7, 48.0, 9.4, 33.7, and 0.3 cm^{-1}, respectively (Supplementary Table S2). The A_1^3, A_1^4, and A_1^5 modes displayed anomalous behavior because the bandwidths of the Davydov splitting peaks in the A_1 mode were larger than those of A_1^1 and A_1^2.

Just Accepted

Our experimental Raman spectroscopy provided direct evidence for anomalous Davydov splitting to a certain extent. In the ML $MoSi_2N_4$ Raman spectrum acquired under 633 nm excitation, we identify a broad band (P12, highlighted in red) at 630-710 cm^{-1} likely originating from the pronounced Davydov splitting of the A_1^3 mode (Fig. 4e). This band is attributed to the densely packed Davydov- split components of the A_1^3 and A_1^4 modes, as supported by the following evidence. Due to the C_{3v} symmetry of 3R-phase MSi_2N_4, all Davydov splitting components are A_1 modes and Raman-active. The corresponding atomic displacement patterns for the layered structure of A_1^3 and A_1^4 were illustrated in Fig. S19 (b). The polarization- dependent spectra (Fig. 4g) show that this broad band strictly follows the polarization selection rules of the A_1 mode, in agreement with group theory predictions. Within the spectral window of 630-710 cm^{-1}, an N-layer sample is therefore expected to produce 2N Davydov splitting components. This behavior differs from 2H-phase TMDs due to D_{3h} symmetry. Only half of the split components are Raman-active in the 2H phase TMD, and the remainder are infrared-active [5]. The calculated frequencies of the A_1^3 and A_1^4 modes of $MoSi_2N_4$ are 685.7 and 694.9 cm^{-1}, respectively, indicating that the two modes may overlap. Therefore, Davydov splitting components of A_1^3 and A_1^4 of $MoSi_2N_4$ appeared too dense to distinguish and formed a continuous band. A similar phenomenon is observed in the experimental Raman data for ML WSi_2N_4, as indicated by the P9 peak (Fig. 4f, highlighted in blue). These findings are consistent with prior theoretical work by A. S. Oreshonkov et al., which reported the same results in the calculated phonon dispersion curves of 2H-phase bulk $MoSi_2N_4$ [7].

An alternative origin of the 630-710 cm^{-1} region of ML $MoSi_2N_4$ was considered: a second-order scattering band 2LA(K) (705.1 cm^{-1}). However, in ML WSi_2N_4, the 2LA(K) peak (539.5 cm^{-1}) is far from the Davydov splitting region (640-720 cm^{-1}). Therefore, the second-order scattering band 2LA(K) can be excluded. This further confirms the presence of an anomalous Davydov splitting in 3R-phase WSi_2N_4.

While the definitive origin of the 630-720 cm^{-1} spectral region may involve

Just Accepted

overlapping contributions from both Davydov splitting components and higher-order scattering in 3R-phase $MoSi_2N_4$, the unique vibrational behavior of MSi_2N_4 implies that the interlayer coupling behavior may be different from that of classical vdW materials.

Just Accepted

Supplementary Note 5. The evaluation of defect concentration by Raman characteristic peak intensity ratio

Previous works demonstrate that the intensity ratio of the first-order Raman peaks to defect-activated peaks (I_X/I_D) is a semi-quantitative indicator in 2D materials [8-10]. In our experiments, He^+ ion irradiation allowed defects to be introduced controllably by varying the irradiation dose. The average interdefect distance L_D is defined as $L_D = C/\sqrt{\sigma}$, where σ and C are the irradiation dose and He^+- ion irradiation damage constant [8]. As shown in Fig. S28a~d, the intensity ratios of A_1^1/LA(K), A_1^1/E^4(K), E^4/LA(K), and E^4/E^4(K) of ML $MoSi_2N_4$ under 532 nm excitation all decrease with increasing defect concentration. These ratios exhibit a reasonable linear correlation with the logarithmic function of L_D (Fig. S28e). Meanwhile, the intensity ratio $I(A_1^1)/I(LA(K))$ under 633 nm excitation shows an ideal linear relationship with L_D in Fig. S28f. These results demonstrate that the intensity ratios of the first- order Raman peaks to defect- activated peaks provide the possibility for qualitative evaluation of defect concentration under both resonant and non- resonant conditions.

Just Accepted

Supplementary Note 6. Laser heating effect on Raman spectra of MSi_2N_4

To account for potential laser heating effects, we collected Raman spectra of 1L $MoSi_2N_4$ and ML WSi_2N_4 under 532 nm with laser powers from 93 to 930 μW. Although the $A_1'^1$ mode exhibits a stronger temperature sensitivity [11], the peak positions of A_1^1, A_1^4, $A_1'^1$, $A_1'^3$ and LA(K) modes extracted from the power‑dependent spectra (Fig. S30) show no discernible shift as the laser power increases. This indicates that, within the power range of 93-930 μW, laser‑induced heating does not cause measurable peak‑position shift. Even though the laser power increases from 0.13 mW to 3.00 mW, the shift of $A_1'^1$ mode is less than 2 cm^{-1} for the suspended monolayer $MoSi_2N_4$ [11].

Just Accepted

Supplementary Note 7. Measurement method of angle- resolved polarized Raman spectroscopy

Angle- resolved polarized Raman spectroscopy was employed to assign the vibrational modes and determine the crystallographic orientation (see Fig. S12 for the optical path diagram). In the linearly polarized configuration, two half- wave plates (P1 and P2) are inserted into the optical path. P1 was placed in the excitation path and rotated from 0° to 360° in 10° increments to continuously vary the polarization direction of the incident laser, while P2 was fixed in the collection path to serve as an analyzer. For circularly polarized measurements, an additional quarter- wave plate (P3) was inserted above the objective to convert the linearly polarized incident beam to circular polarization. By rotating P1, the polarization state of the incident light could be tuned, while P2 and P3 together acted as a fixed analyzer in the collection path.

Just Accepted

References

[1] Miller, B.; Lindlau, J.; Bommert, M.; Neumann, A.; Yamaguchi, H.; Holleitner, A.; Högele, A.; Wurstbauer, U. Tuning the Fröhlich exciton-phonon scattering in monolayer MoS_2. *Nat. Commun.* **2019**, 10, 807.

[2] Ferrari, A. C.; Meyer, J. C.; Scardaci, V.; Casiraghi, C.; Lazzeri, M.; Mauri, F.; Piscanec, S.; Jiang, D.; Novoselov, K. S.; Roth, S.; Geim, A. K. Raman Spectrum of Graphene and Graphene Layers. *Phys. Rev. Lett.* **2006**, *97*, 187401.

[3] Rojas, F. S.; Ojeda, C. B.; Pavon, J. M. C. Derivative ultraviolet—visible region absorption spectrophotometry and its analytical applications. *Talanta* **1988**, *35* (10), 753.

[4] Liu, H.-L.; Yang, T.; Tatsumi, Y.; Zhang, Y.; Dong, B.; Guo, H.; Zhang, Z.; Kumamoto, Y.; Li, M.-Y.; Li, L.-J.; Saito, R.; Kawata, S. Deep-ultraviolet Raman scattering spectroscopy of monolayer WS_2. *Sci. Rep.* **2018**, *8*, 11398.

[5] Song, Q. J.; Tan, Q. H.; Zhang, X.; Wu, J. B.; Sheng, B. W.; Wan, Y.; Wang, X. Q.; Dai, L.; Tan, P. Physical origin of Davydov splitting and resonant Raman spectroscopy of Davydov components in multilayer $MoTe_2$. *Phys. Rev. B* **2016**, *93*, 115409.

[6] Zhao, Y.; Luo, X.; Li, H.; Zhang, J.; Araujo, P. T.; Gan, C. K.; Wu, J.; Zhang, H.; Quek, S. Y.; Dresselhaus, M. S.; Xiong, Q. Interlayer breathing and shear modes in few-trilayer MoS_2 and WSe_2. *Nano Lett.* **2013**, *13*, 1007-1015.

[7] Oreshonkov, A. S.; Sukhanova, E. V.; Popov, Z. I. Phonon dynamics in $MoSi_2N_4$: insights from DFT calculations. *Phys. Chem. Chem. Phys.* **2023**, *25*, 29831-29841.

[8] Mignuzzi, S.; Pollard, A. J.; Bonini, N.; Brennan, B.; Gilmore, I. S.; Pimenta, M. A.; Richards, D.; Roy, D. Effect of disorder on Raman scattering of single-layer MoS_2. *Phys. Rev. B* **2015**, *91*, 195411.

[9] Lucchese, M. M.; Stavale, F.; Ferreira, E. H. M.; Vilani, C.; Moutinho, M. V. O.; Capaz, R. B.; Achete, C. A.; Jorio, A. Quantifying ion-induced defects and Raman relaxation length in graphene. *Carbon* **2010**, *48* (5), 1592.

[10] Moses Badlyan, N.; Quincke, M.; Kaiser, U.; Maultzsch, J. TEM-processed defect densities in single-layer TMDCs and their substrate-dependent signature in PL and Raman spectroscopy. *Nanotechnology* **2024**, *35*, 435001.

Just Accepted

[11] He, C.; Xu, C.; Chen, C.; Tong, J.; Zhou, T.; Sun, S.; Liu, Z.; Cheng, H.-M.; Ren, W. Unusually high thermal conductivity in suspended monolayer $MoSi_2N_4$. *Nat. Commun.* **2024**, *15*, 4832.

Just Accepted